ornl

ORNL/TM-12864

OAK RIDGE
NATIONAL
LABORATORY

MARTIN MARIETTA

Experimental Investigations of Sensor-Based Surface Following Performed by a Mobile Manipulator

David B. Reister
Michael A. Unseren
James E. Baker
François G. Pin

MANAGED BY
MARTIN MARIETTA ENERGY SYSTEMS, INC.
FOR THE UNITED STATES
DEPARTMENT OF ENERGY

ORNL/TM-12864

Engineering Physics and Mathematics Division

EXPERIMENTAL INVESTIGATIONS OF SENSOR-BASED SURFACE FOLLOWING PERFORMED BY A MOBILE MANIPULATOR

David B. Reister, Michael A. Unseren, James E. Baker, and François G. Pin

DATE PUBLISHED — October 1994

Research sponsored by the
Engineering Research Program
Office of Basic Energy
Sciences
U.S. Department of Energy

Prepared by the
OAK RIDGE NATIONAL LABORATORY
Oak Ridge, Tennessee 37831
managed by
MARTIN MARIETTA ENERGY SYSTEMS, INC.
for the
U.S. DEPARTMENT OF ENERGY
under contract DE-AC05-84OR21400

CONTENTS

LIST OF FIGURES

LIST OF FIGURES (cont'd)

ABSTRACT

We discuss a series of surface following experiments using a range finder mounted on the end of an arm that is mounted on a vehicle. The goal is to keep the range finder at a fixed distance from an unknown surface and to keep the orientation of the range finder perpendicular to the surface. During the experiments, the vehicle moves along a predefined trajectory while planning software determines the position and orientation of the arm. To keep the range finder perpendicular to the surface, the planning software calculates the surface normal for the unknown surface. We assume that the unknown surface is a cylinder (the surface depends on x and y but does not depend on z). To calculate the surface normal, the planning software must calculate the locations (x, y) of points on the surface in world coordinates. The calculation requires data on the position and orientation of the vehicle, the position and orientation of the arm, and the distance from the range finder to the surface.

We discuss four series of experiments. During the first series of experiments, the calculated surface normal values had large high frequency random variations. A filter was used to produce an average value for the surface normal and we limited the rate of change in the yaw angle target for the arm. We performed the experiment for a variety of concave and convex surfaces. While the experiments were qualitative successes, the measured distance to the surface was significantly different than the target. The distance errors were systematic, low frequency, and had magnitudes up to 25 mm.

During the second series of experiments, we reduced the variations in the calculated surface normal values. While reviewing the data collected while following the surface of a barrel, we found that the radius of the calculated surface was significantly different than the measured radius of the barrel. We performed a third series of experiments with the arm in a fixed position and determined that the position and orientation errors in the dead reckoning system for the vehicle was the source of the radii errors.

Our objective during the fourth series of experiments was to reduce the distance errors. Although we introduced a correction term, we were unable to significantly reduce the distance errors. We concluded that the experiment must be redesigned to reduce the errors in the calculations of points on the unknown surface.

1. INTRODUCTION

Mobile manipulators (manipulators mounted on vehicles) are attracting significant interest in the industrial, military, and public service communities because of the substantial increases in task capabilities and efficiency that result from their large-scale mobility combined with manipulation abilities. Our long term goal is to develop mobile manipulator systems that can autonomously perform site characterization. There are many highly contaminated facilities at Department of Energy sites that must eventually undergo some form of Decontamination and Decommissioning (D&D). D&D operations include disassembly of process equipment, cutting pipes, and transport of pipe and equipment out of hot cells. Before D&D, the contaminated facility must be surveyed to determine its current characteristics (including: geometry, materials, and radiation levels).

This paper discusses an early milestone on the path to our long term goal. We report on a series of experiments with three interacting systems: a vehicle, an arm, and a range finder. The goal is to keep the range finder at a fixed distance from an unknown surface and to keep the orientation of the range finder perpendicular to the surface. During the experiments, the vehicle moves along a predefined path while planning software determines the target position and orientation of the arm.

The next section provides more details on the three interacting systems and discusses the calculations that are performed by the planning software. The third section discusses the four series of experiments. The fourth section details our conclusions. Further experimental details are provided in the two appendices.

2. EXPERIMENTAL CONFIGURATION

HERMIES-III [1],[2] is a human-size mobile manipulator test-bed (see Fig. 1) incorporating the seven degree-of-freedom (DOF) CESARm research manipulator on a four DOF vehicle (with two independently-driven and steerable wheels). The software and hardware configuration of HERMIES-III utilizes the HELIX communication protocol [3], allowing for a fully distributed and message passing modular control system on several connected VMEbus racks. The vehicle's control drivers and sensor-feedback odometry modules operate at 20 Hz. The redundancy resolution module for the CESARm includes 3-D position and 3-D orientation control and utilizes a minimum Euclidean norm-based algorithm running at 50 Hz on a 68020 processor [4]. The forward kinematics calculations run at 150 Hz on another 68020 processor.

For the experiments, a very accurate (0.05 mm precision), single point LED triangulation-type range finder [5],[6] was held in the gripper of the CESARm (see Fig. 1). The vehicle was assigned to perform a specified trajectory on the floor, while the CESARm end-effector's task was to follow an *a priori* unknown surface, maintaining both constant distance and constant orientation from the surface using the range finder data. Because the LED range sensor is unidirectional and provides data from a single beam, estimation of the surface normal (necessary to maintain constant orientation) required an estimate of the absolute displacement of the measurement point on the surface expressed in the reference (or world) coordinate system. This estimation therefore required propagation of position and orientation estimates through the entire vehicle-arm-gripper-sensor-beam chain.

2.1. SURFACE CALCULATION

The distance sensor is located on the end-effector of the CESARm that is mounted on the mobile vehicle of HERMIES-III. The goal is to measure the curvature of an arbitrary cylindrical surface and keep the sensor at a fixed distance from the surface and normal to the surface. To measure the curvature of the surface, we must measure points on the surface in the world coordinate system. The system has three coordinate systems: world, vehicle, and arm (see Fig. 2). In this subsection we show how the measured data is used to calculate a point on the surface in each of the coordinate systems.

Our objective is to calculate a point on the surface of an object in the world coordinate system (x_s, y_s). In the experiments dealt with here, we assume that the shape of the object does not depend on the z coordinate (that the unknown object is a cylinder with an arbitrary shape in the xy plane). Thus, all of our calculations will be in 2D geometry. The measured data are the distance to the surface (D), the configuration of the last link of the manipulator measured in the arm coordinate system (x_b, y_b, Θ_p), and the location of the vehicle in the world coordinate system (x_p, y_p, ϕ_p). The arm is controlled in 3D space $(x, y, z,$ roll, pitch, yaw) and θ_b is the measured yaw angle.

The base of the arm is attached to the vehicle. Thus, the transformation between the arm coordinates and the vehicle coordinates does not vary. Unfortunately, the

transformation requires both a translation and a rotation of 180 degrees. If (x_h, y_h, θ_h) is the configuration of the last link of the manipulator measured in the vehicle coordinate system:

$$x_h = -x_b + \mathrm{B} \tag{1}$$

$$y_h = -y_b \tag{2}$$

$$\theta_h = \theta_b - \pi/2 \tag{3}$$

where B is the x coordinate of the arm base in the vehicle coordinate system ($B = 0.574$ meters). In the home position for the arm, (x_b, y_b, θ_b) = (-0.880, -0.356, $\pi/2$) and (x_h, y_h, θ_h) = (1.454, 0.365, 0.0).

To reach the surface of the object in the vehicle coordinate system (x_d, y_d), we travel in the θ_h direction by the sum of the length of the distance sensor (L = 0.062 meters) and the measured distance (D):

$$x_d = x_h + (D + \mathrm{L}) \cos \theta_h \tag{4}$$

$$y_d = y_h + (D + \mathrm{L}) \sin \theta_h \tag{5}$$

To calculate a point (x_s, y_s) on the surface of the object in the world coordinate system, we transform the coordinates from the vehicle reference frame to the world reference frame:

$$x_s = x_p + x_d \cos \phi_p - y_d \sin \phi_p \tag{6}$$

$$y_s = y_p + x_d \sin \phi_p + y_d \cos \phi_p \tag{7}$$

Note that we have used all of the measured data $[D, (x_b, y_b, \theta_b)$, and $(x_p, y_p, \phi_p)]$ to calculate the location of the point (x_s, y_s) that we have measured on the surface.

2.2. SURFACE NORMAL CALCULATION

The location of the points on the surface are calculated at 100 Hz (100 Hz is the nominal rate. The measured rate is about 75 Hz). At 10 Hz, we would like to calculate the surface normal and the arm goal. To calculate the surface normal, we fit a polynomial to the surface points and calculate the slope of the curve. There are tradeoffs in choosing the order of the polynomial and the number of data points to use to estimate the parameters. A higher order polynomial (cubic or quadratic) has more parameters and requires more data points to estimate the parameters. Furthermore, a high order polynomial might not provide a good fit to a surface with discontinuous surface normals (e.g., a box). Our goal is to obtain the best estimate of the surface normal in a small neighborhood of the currently measured point on the surface. Thus, we would like to fit a curve with a small number of

parameters using a small number of data points. We decided to fit a line using M points, where M is a user-defined parameter that can be adjusted to improve performance.

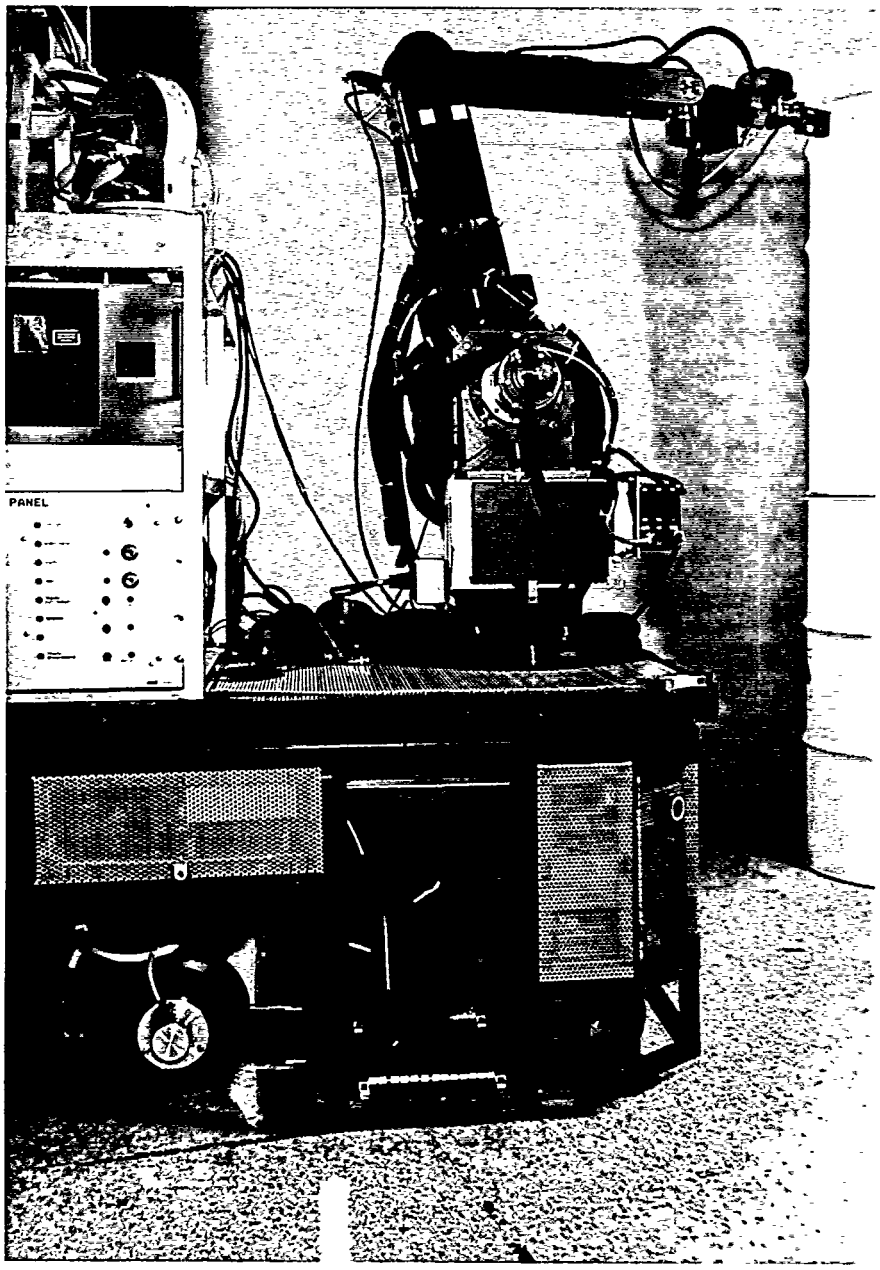

Fig. 1. The HERMIES-III robot follows an arbitrary unknown surface.

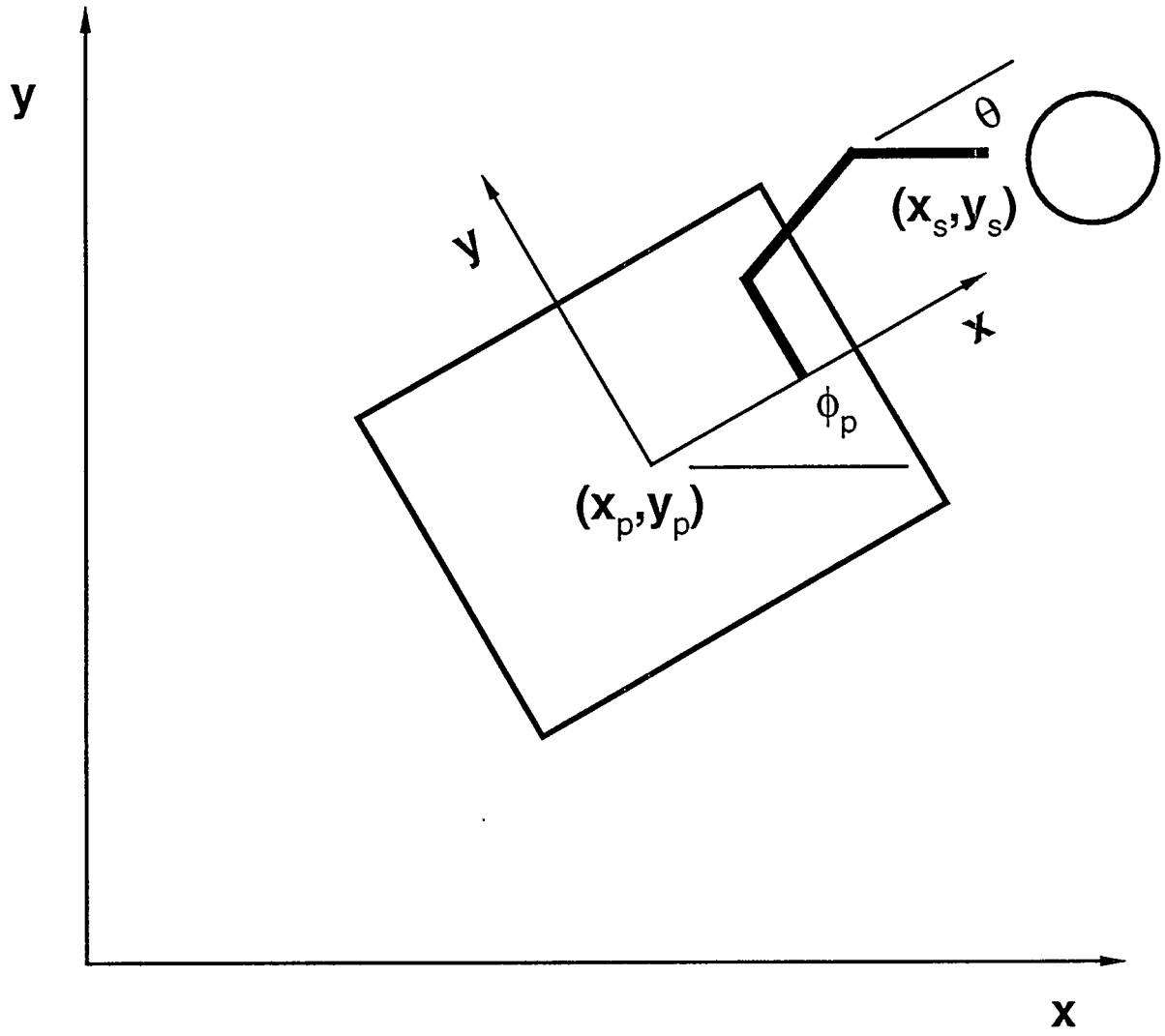

Fig. 2. The experimental configuration.

We have performed four series of experiments: the first in 1992 and the other three in 1993 and January 1994. During the first series of experiments, we performed ten distance measurements each cycle (at 100 Hz) and averaged them. Using the average distance, we calculated a point on the surface of the object. Every tenth cycle (at 10 Hz), we fitted a line to the 10 data points. Thus, M=10 for the first series of experiments.

During the second (and subsequent) series of experiments, we performed four distance measurements each cycle. For each of the four measurements, we calculated a point on the surface of the object. Every tenth cycle (at 10 Hz), we fitted a line to N sets of 40 data points (for the data in this paper, N=5). Thus, M=40 N=200 for the second series of experiments.

Given M points on the surface, we determine the maximum and minimum values for each of their coordinates, x and y. If the spread in x is greater than the spread in y, we assume that $y = f(x)$. Otherwise, we assume that $x = f(y)$. The maximum speed for the

vehicle is 0.45 meters/second. Thus, the maximum distance traveled in 0.1 seconds is 0.045 meters. If the maximum spread is less than 0.003 N meters, we do not calculate the surface normal. Otherwise, we use least squares to fit a line to the data points.

Let ψ be the normal to the line and let θ_s be the surface normal in the vehicle coordinate system, then:

$$\theta_s = \psi - \phi_p \tag{8}$$

Typical experimental values for the surface normal (θ_s) for the first series of experiments are displayed in Fig. 3.

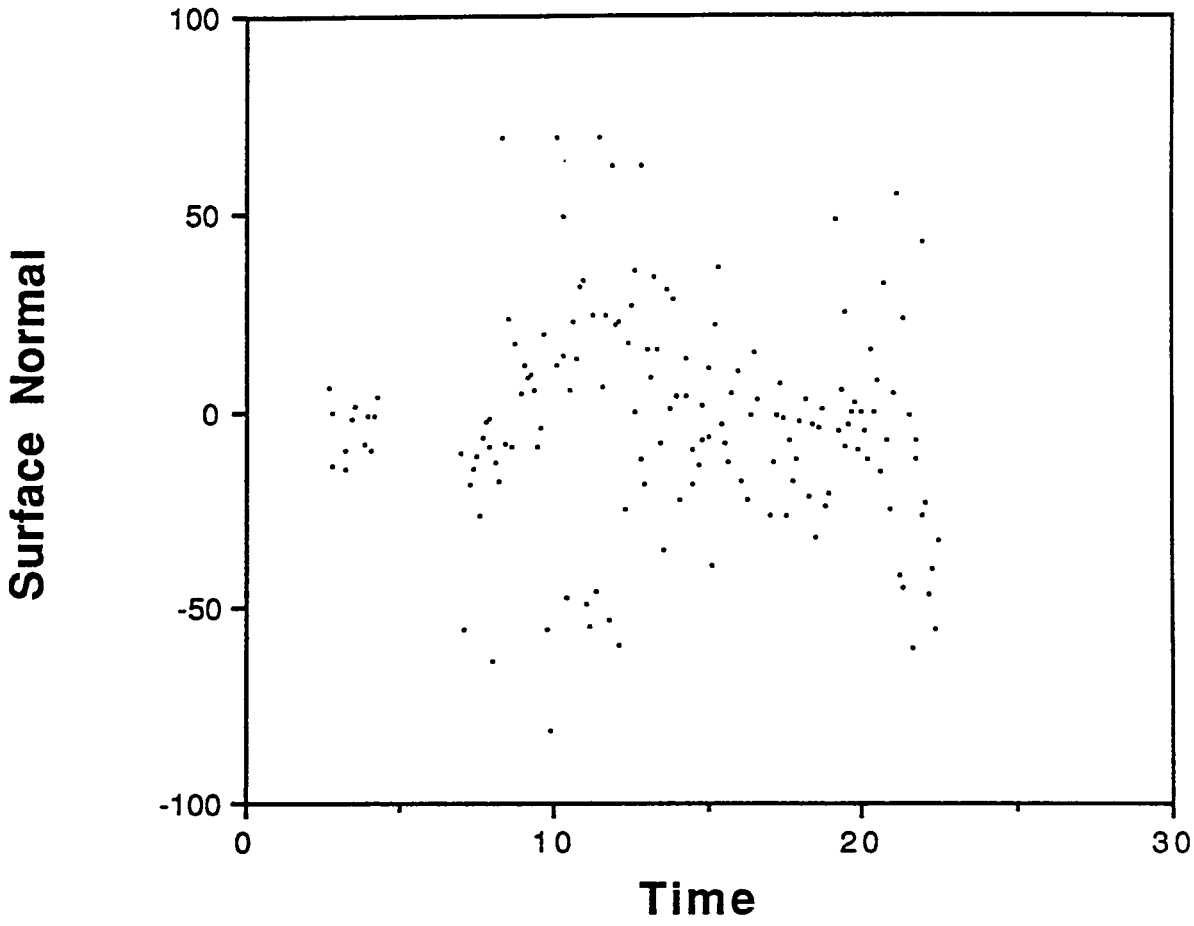

Fig. 3. Calculated values for the surface normal for the first experiment. The units are degrees.

It is clear that the values displayed in Fig. 3 are much too variable or noisy to be fed as an input target to the manipulator. When the input to the arm has high frequency noise, the arm will oscillate. To provide a smooth input to the arm, we filtered the calculated values of the surface normal (θ_s). Let θ_g be a running average of the calculated values for the surface normal:

$$\theta_g(t+1) = (1-\mu)\,\theta_g(t) + \mu\,\theta_s(t) \tag{9}$$

When the parameter μ is 1.0, the average value is equal to the input ($\theta_g = \theta_s$). When the parameter μ is 0.0, the average is a constant that does not depend on the input. For the first series of experiments, $\mu = 0.1$. For the second (and subsequent) series of experiments, $\mu = 0.5$.

Let θ_c be the target value for the orientation of the arm. We let the target track the average value of the surface normal. Let ε be the difference between the target and the average value: $\varepsilon = \theta_g - \theta_c$. We limited the allowable rate of change ε to a given value δ. Thus, if $\varepsilon > \delta$, then $\varepsilon = \delta$ and if $\varepsilon < -\delta$, then $\varepsilon = -\delta$. Finally:

$$\theta_c(t+1) = \theta_c(t) + \varepsilon \tag{10}$$

For the first series of experiments, δ = 0.01. For the second (and subsequent) series of experiments, $\delta = 0.03$. Thus, the four parameters (M, N, μ, and δ) can be used to smooth the time varying input to the arm.

2.3. ARM GOAL POSITION CALCULATION

The calculation of a goal for the arm is illustrated in Fig. 4. The current orientation of the arm is θ. In the current position, the schematic follows the arm from the wrist (w), to the hand (h), and past the surface detector (d) to the surface (s). The figure also displays the goal configuration of the arm (at orientation θ_c). Given the orientation, the goal for the hand (x_c, y_c) is calculated as:

$$x_c = x_d - (D_g + \mathrm{L}) \cos\theta_c \tag{11}$$

$$y_c = y_d - (D_g + \mathrm{L}) \sin\theta_c \tag{12}$$

where the desired value for the distance is $D_g = 0.102$ meters in the experiments described here.

The goal for the hand depends on a base point on the surface of the object in the vehicle coordinate system (x_d, y_d). For the first series of experiments, we used the most recent value of (x_d, y_d) as the base point. However, the arm is compliant and oscillations in the point on the surface can be amplified if they are passed to the goal for the arm. To reduce this feedback in the second (and subsequent) series of experiments, we fitted a line to the last 200 values of x_d to estimate $x_d = f(t)$ and used the most recent point on the line as the base point. We used the same procedure to determine the y_d base point.

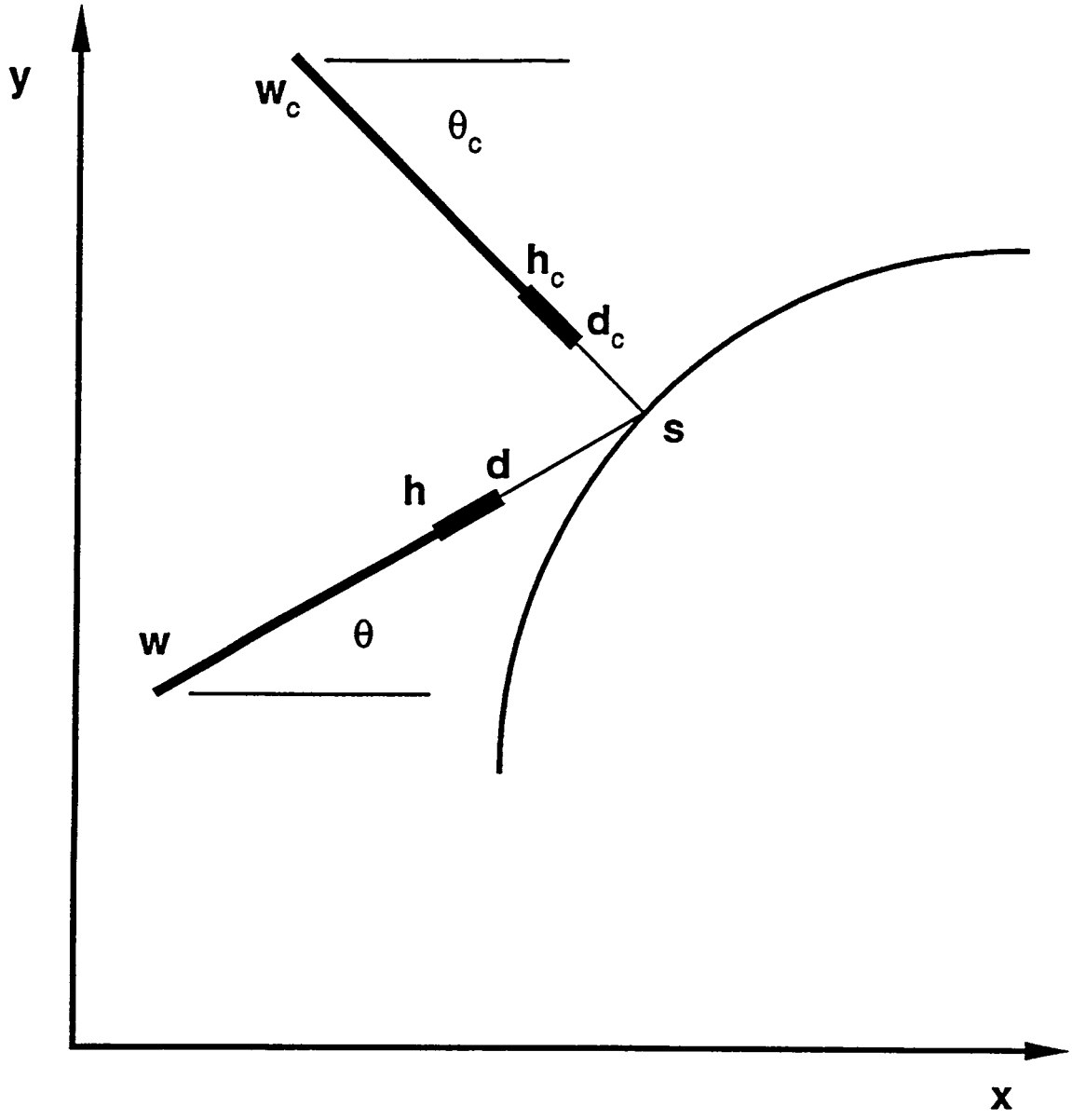

Fig. 4. The calculation of the next goal for the arm.

3. EXPERIMENTAL RESULTS AND DISCUSSION

In this section, we discuss four series of experiments. During the first series of experiments, the calculated surface normal values had large high frequency random variations (see Fig. 3). A filter was used to produce an average value for the surface normal and we limited the rate of change in the yaw angle target for the arm. We performed the experiment for a variety of concave and convex surfaces. While the experiments were qualitative successes, the measured distance to the surface was significantly different than the target. The distance errors were systematic, low frequency, and had magnitudes up to 25 mm.

During the second series of experiments, we reduced the variations in the calculated surface normal values. While reviewing the data collected while following the surface of a barrel, we found that the radius of the calculated surface was significantly different than the measured radius of the barrel. We performed a third series of experiments with the arm in a fixed position and determined that the position and orientation errors in the dead reckoning system for the vehicle was the source of the radii errors.

Our objective during the fourth series of experiments was to reduce the distance errors. Although we introduced a correction term, we were unable to significantly reduce the distance errors. We concluded that the experiment must be redesigned to reduce the errors in the calculations of points on the unknown surface.

3.1. FIRST EXPERIMENT

In the first experiment, the arm began in the center of a curved surface. During the experiment, the vehicle made a linear motion to the right, made a linear motion to the left past the starting point, and made a linear motion to the right to the starting point. Figure 5 displays the distance measurements from the range finder during the first experiment. The goal was to maintain a distance of 0.102 meters. Clearly, the measured values show that the end-effector can be more than two centimeters from the goal. The low frequency of the curve would seem to indicate that an error accumulation takes place over time in the system. The source of error could be either in the data that are produced by the three systems (vehicle, arm, and range finder) or in the calculations that are performed by the planning software. We have checked the software repeatedly and will assume that the software is not the error source.

To explore the sources of the low frequency errors in Fig. 5, we will examine each of the potential errors in the calculation. The range finder produces valid readings within 40 mm of the desired distance. Since all of the distance measurements in Fig. 5 are within 40 mm of the desired distance, the distance measurements are valid.

Figure 6 is a plot of the points (x_s, y_s) on the surface of the barrel calculated in the world reference frame from integration of the measured data over the entire vehicle-arm-sensor chain. There is significant noise in the data and both the low and high frequency errors can be observed. The very large scattering in the surface normal results which were observed in Fig. 3 correlate with the high frequency variations observed on Fig. 6.

A large part of the low frequency errors, however, cannot be corrected through any type of filtering. Although the reckoner for the vehicle can produce slight integration errors, the major sources of the large observed errors in Fig. 6 are thought to reside in the rolling contact of the vehicle's wheel on the floor. When moving along a circle, with the two driving wheels steered at different angles, the effective point of contact of the wide rubber-coated wheels varies slightly under the wheels with slight irregularities on the floor. This generates errors in the wheel velocity targets that are calculated to fulfill the rigid body constraint (which exists between the wheels in this configuration). From these errors, slight slippage of the wheels on the floor results, progressively accumulating to large errors, (undetectable with the odometry sensors).

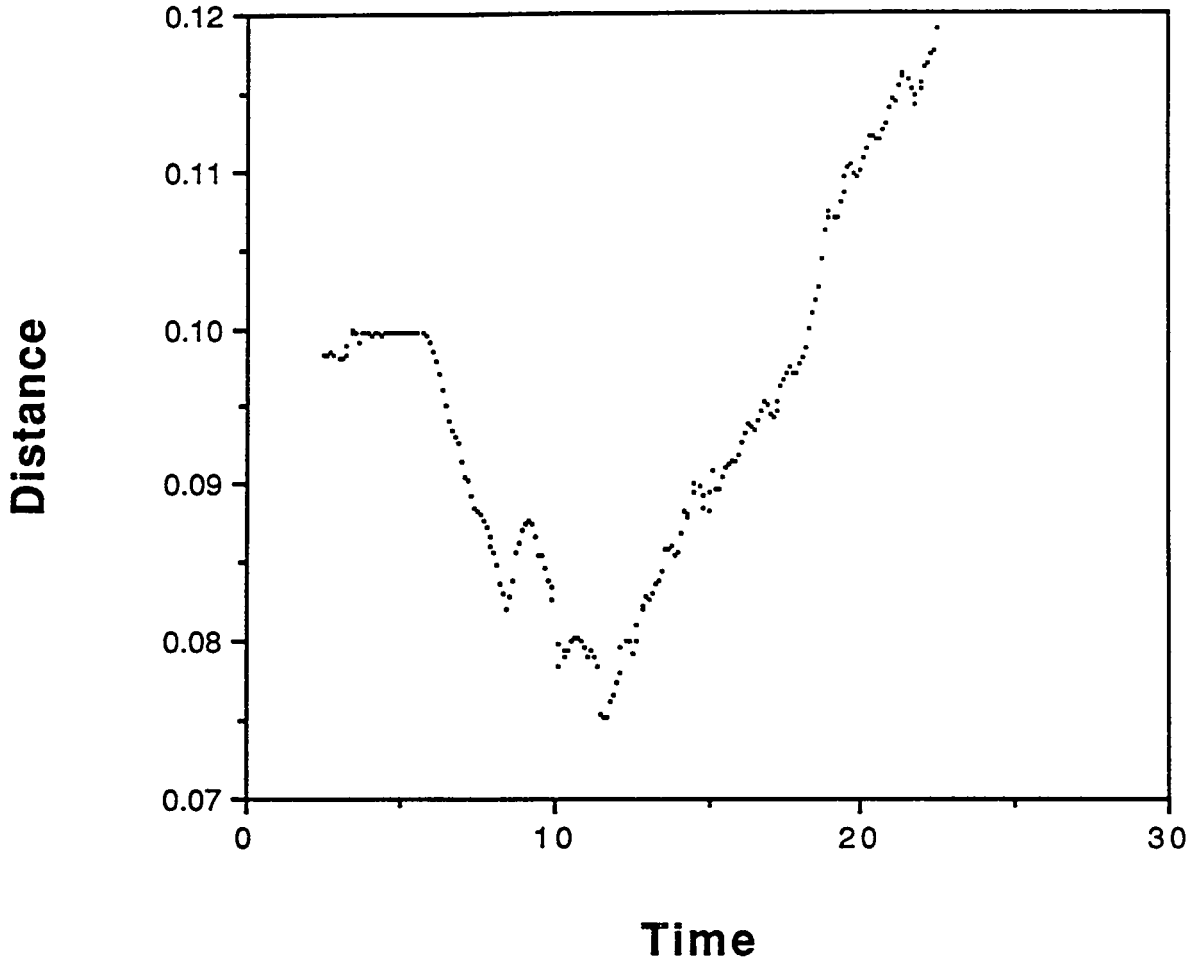

Fig. 5. The distance from the range finder sensor to the unknown surface for the first experiment. The units are meters.

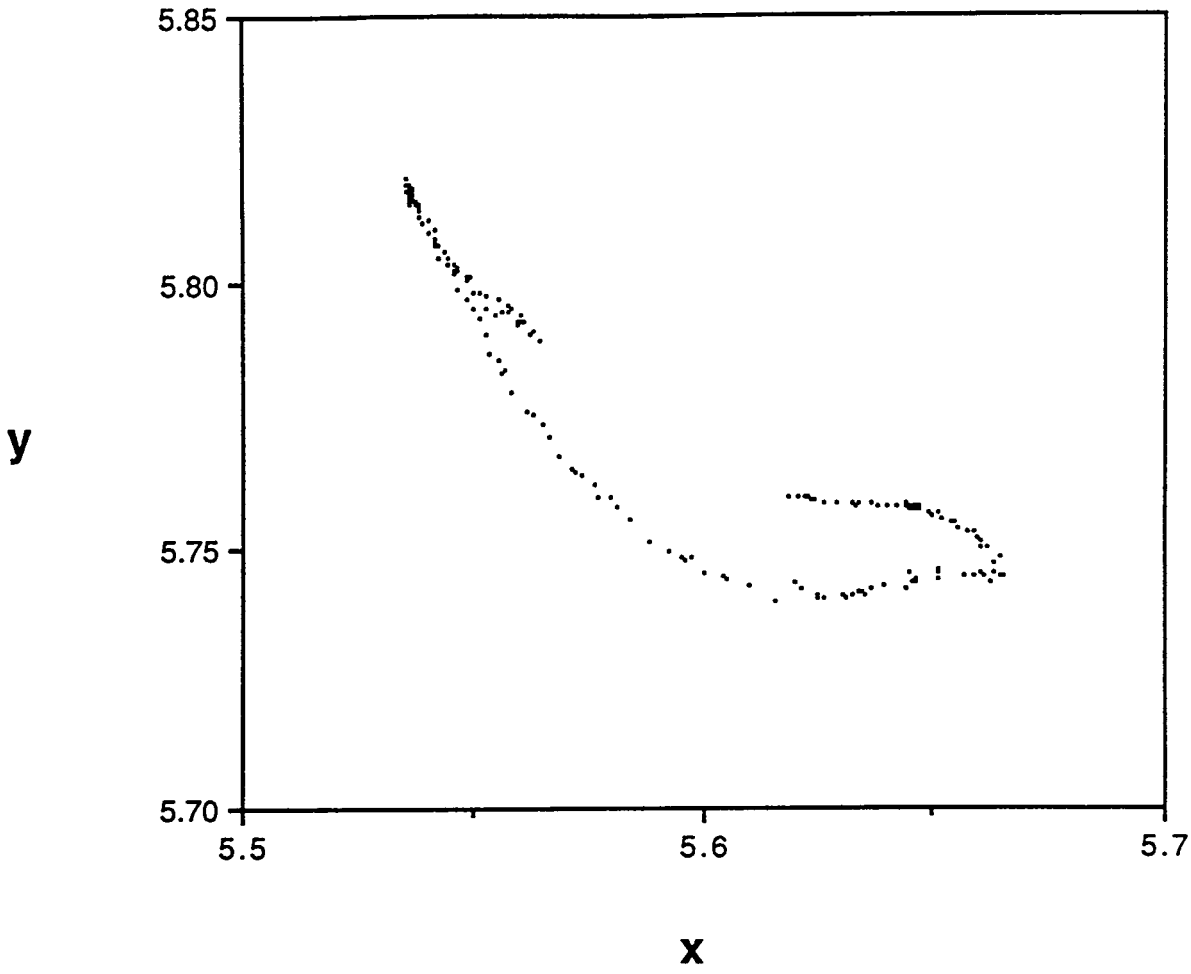

Fig. 6. The calculated position of the unknown surface in the world coordinate system for the first experiment. The units of x and y are meters.

In a first step toward remedying this problem, a composite control architecture which accommodates for violations of the interwheel rigid body kinematic constraints in addition to controlling the position of the vehicle wheel system has recently been developed [7] and has shown dramatic improvements on the vehicle's control accuracy when used on HERMIES-III. However, the composite control architecture does not eliminate the reckoning errors for the position and orientation of the vehicle.

The manipulator arm was also investigated as the possible source of some of the error. The manipulator system consistently follows the target values for both position and orientation as calculated from Eqs. (1) to (12). As an example of this, Fig. 7 displays a

time log of the target ($\theta_c + \pi/2$) and the measured values (θ_b) for the manipulator yaw angle. The targets move smoothly and the measured values follow the targets accurately, with an expected lag in execution of the order of one to two cycles of the 10 Hz calculational scheme. The smooth motion of the yaw targets demonstrates that the filtering parameter (μ) and the velocity bound (δ) produce a smooth signal from the noisy input data in Fig. 3. The time delay between the targets (set points) and the execution, therefore, cannot explain either the low frequency divergences exhibited in Fig. 5 or the large scattering displayed in Fig. 3.

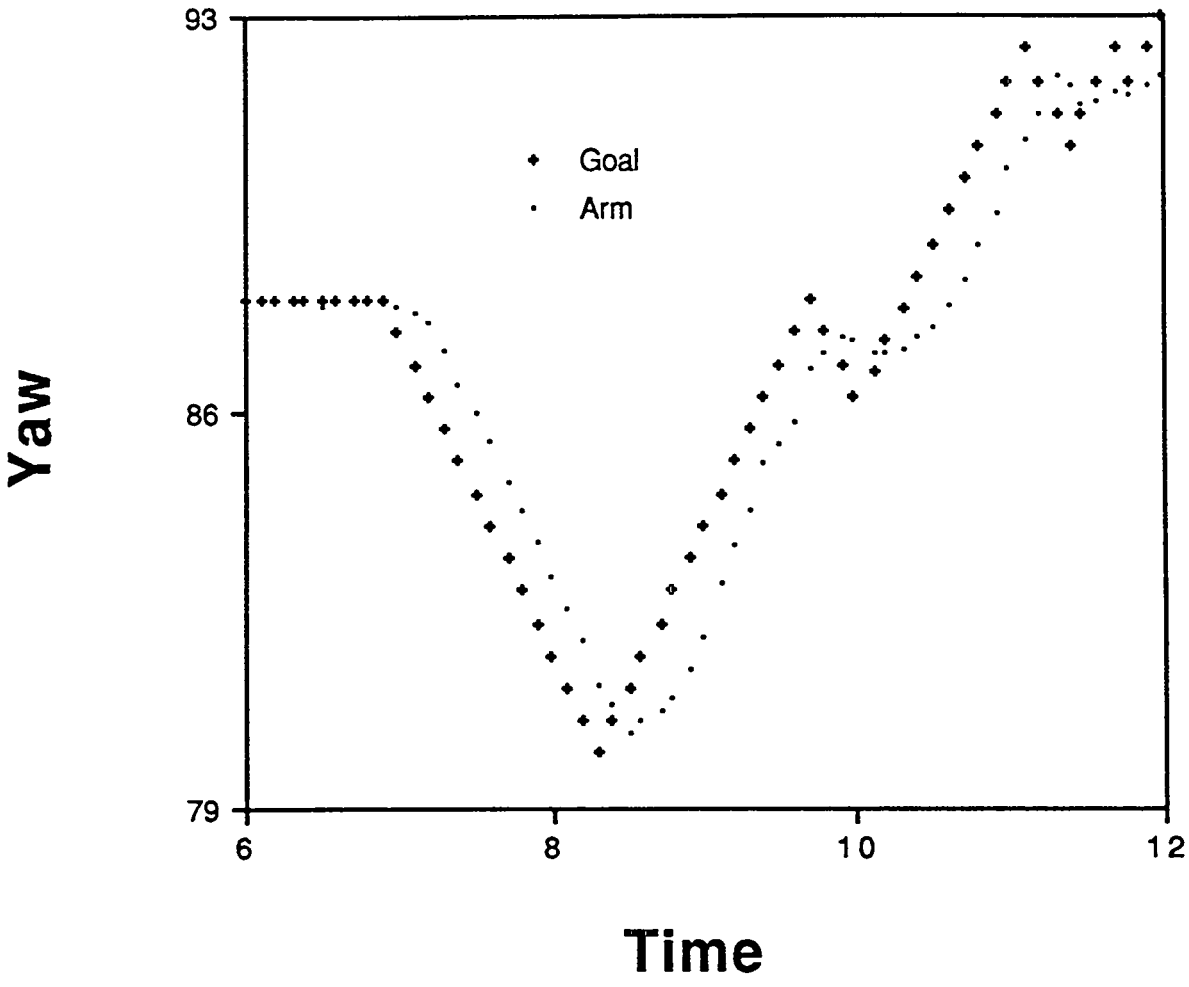

Fig. 7. Target and measured values for the yaw angle for the first experiment. The units are degrees.

The forward kinematics calculations for the arm could be a source of error. We have not attempted to experimentally verify the calculated values for the position and orientation of the arm. The calculation of the goal for the arm is performed in the arm coordinate system (not in the world coordinate system). Thus, errors in the position and orientation of the vehicle may lead to errors in the shape of the surface and errors in the surface normal, however, they should have no impact on the distance error. The distance errors must be caused by errors in the position and orientation of the arm. We will return to this topic in Section 3.4.

3.2. SECOND EXPERIMENT

The motivation for the second series was provided by a quest for the possible sources of errors encountered during the first series, and experimental investigations of the data provided by the range finder. For another project, we used the range finder to measure the distance from a vehicle to the floor and observed unexpected discontinuities in the data (see Appendix A). We performed a series of experiments to investigate the behavior of the Analog to Digital board. We increased the precision of the output from the board and concluded that we should not average the output from the board. With new confidence in the data from the range finder, we decided to initiate the second series of experiments. In the second series of experiments, the vehicle moved in an arc about a barrel and returned to its initial location.

To improve our understanding of the sources of the scatter in the surface normal data in Fig. 3, we collected all of the points on the surface of the barrel for 100 cycles. Typical results are displayed in Fig. 8. Each cycle, we performed four distance measurements and calculated a point on the surface of the barrel. Thus, 400 data points are displayed in the figure. The nominal time for 100 cycles is one second. The actual time to collect the data in Fig. 8 was 1.34 seconds (about 75 Hz). The circles in Fig. 8 are the data that was collected every tenth cycle.

For the first series of experiments, we determined the best line for the data between each pair of circles and obtained the scattered results in Fig. 3. For the second series of experiments, we determined the best line for the data between six circles and obtained the results in Fig. 9. Each line depends on 200 data points. For the next calculation of surface normal, we drop 40 data points and add 40 data points. This method produced much more continuous results than our previous method. It is clear from Fig. 9 that the surface normal calculation does not exhibit the very large scattering observed in Fig. 3.

As mentioned previously, for each set of 200 data points, we determine the spread in x and y. If the maximum spread is less than 15 mm, we do not calculate the surface normal. For the first seven seconds of the data in Fig. 9, the vehicle is not moving enough to generate sufficient spread in the data and we do not calculate the surface normal. The vehicle circles the barrel, stops, and returns. Similarly, during the period when the vehicle stops and reverses direction (from 14 seconds to 17 seconds on Fig. 9), the vehicle is not moving enough to generate sufficient spread in the data.

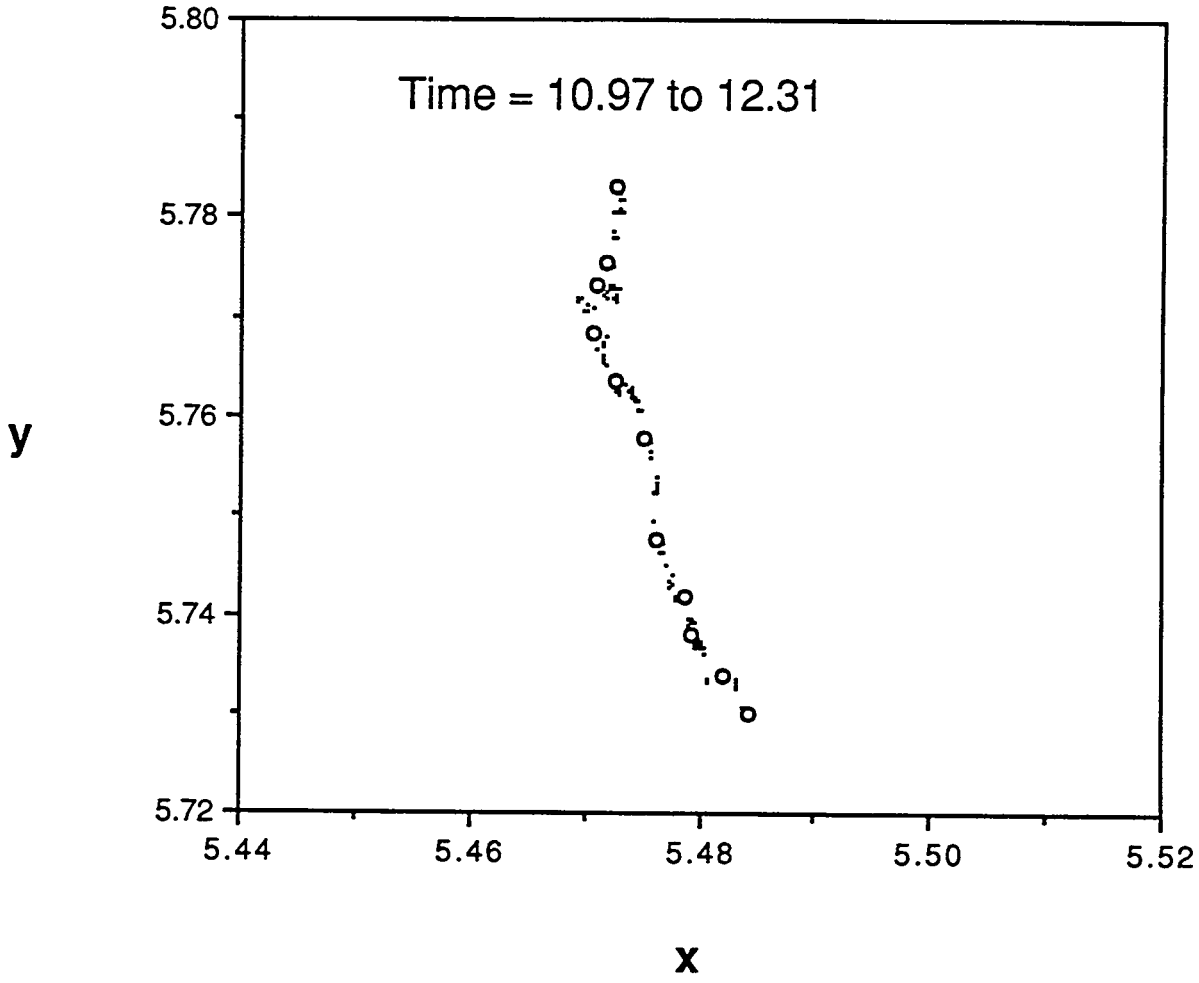

Fig. 8. All of the calculated points on the surface of the barrel in the world coordinate system for 100 cycles. The data identified by a circle were collected every tenth cycle. The units of x and y are meters.

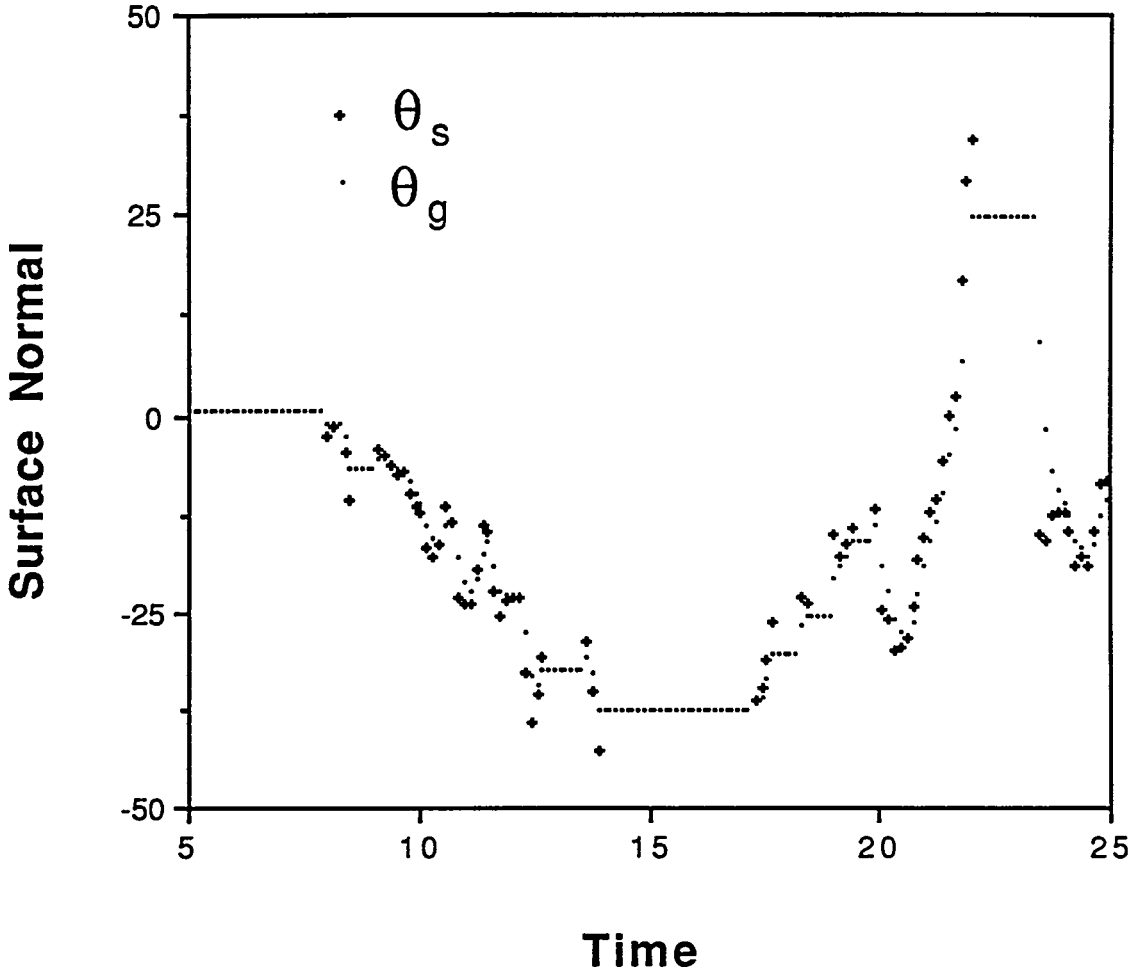

Fig. 9. Calculated values for the surface normal and their average values for the second experiment. The units are degrees.

Figure 10 is a plot of the points on the surface of the barrel. The data in Fig. 10 are much more consistent than the data in Fig. 6. The surface measurements begin at the lower right, follow the barrel to the upper left, and return. The last thirty points (out of 200) are displayed with a new plotting symbol (a small plus) and show the greatest deviation from the initial curve. For the last 30 points, the vehicle has stopped moving. Thus, the deviations may be due to faulty values for the forward kinematics calculations (Denavit-Hartenberg parameters).

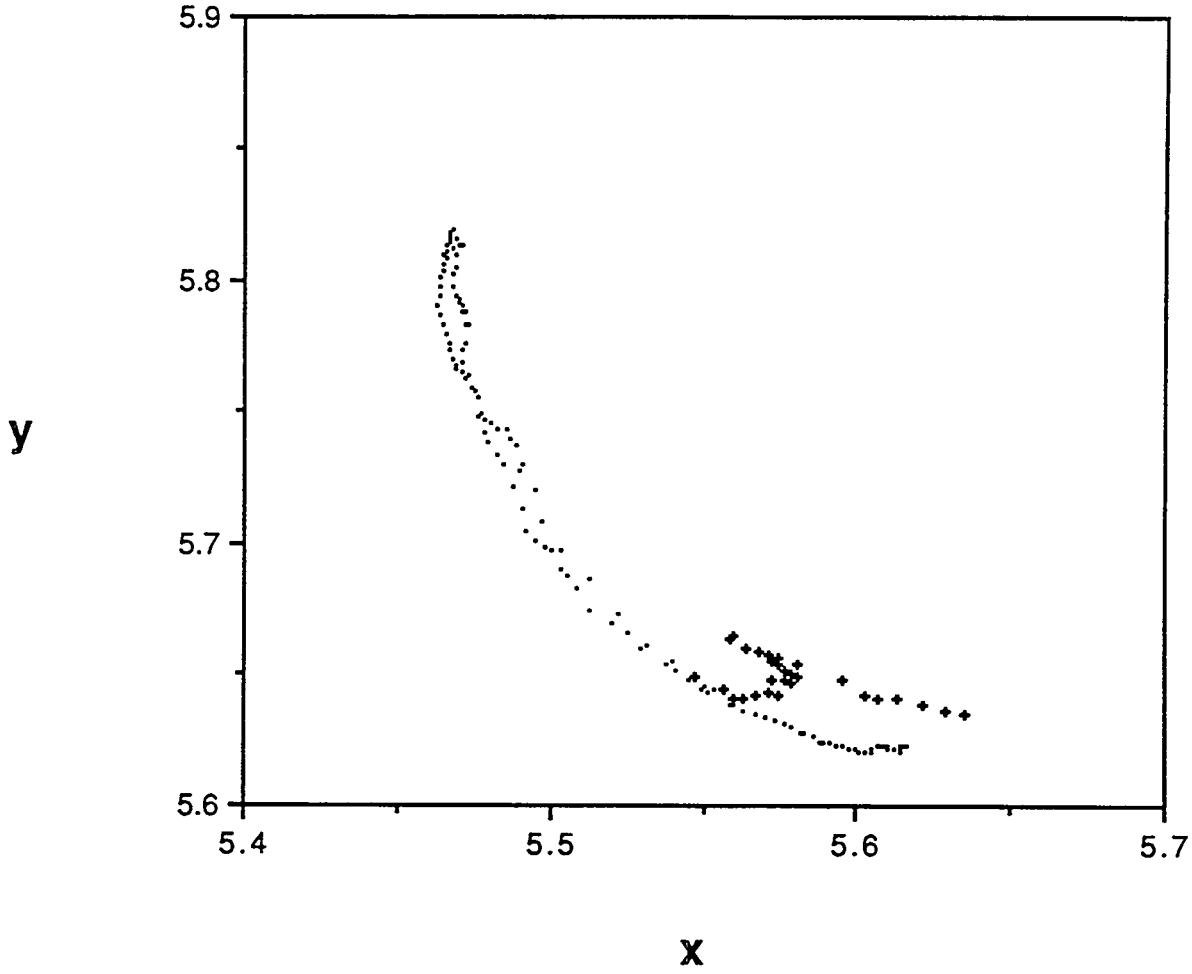

Fig. 10. The calculated position of the unknown surface in the world coordinate system for the second experiment. The units of x and y are meters.

Figure 11 displays a plot of the target and measured values for the yaw angle. The changes in yaw angle are much larger than in Fig. 7. In Fig. 7, the values of the yaw angle are within 10 degrees of the initial value (90 degrees). In Fig. 11, the values decrease from 90 degrees to about 53 degrees before increasing to 102 degrees. For the second series of experiments, the velocity bound (δ) was increased by a factor of 3 (from $\delta = 0.01$ to $\delta = 0.03$). The improved response is visible during the decrease in yaw angle in Fig. 11. Several times, the target catches the running average and stops decreasing.

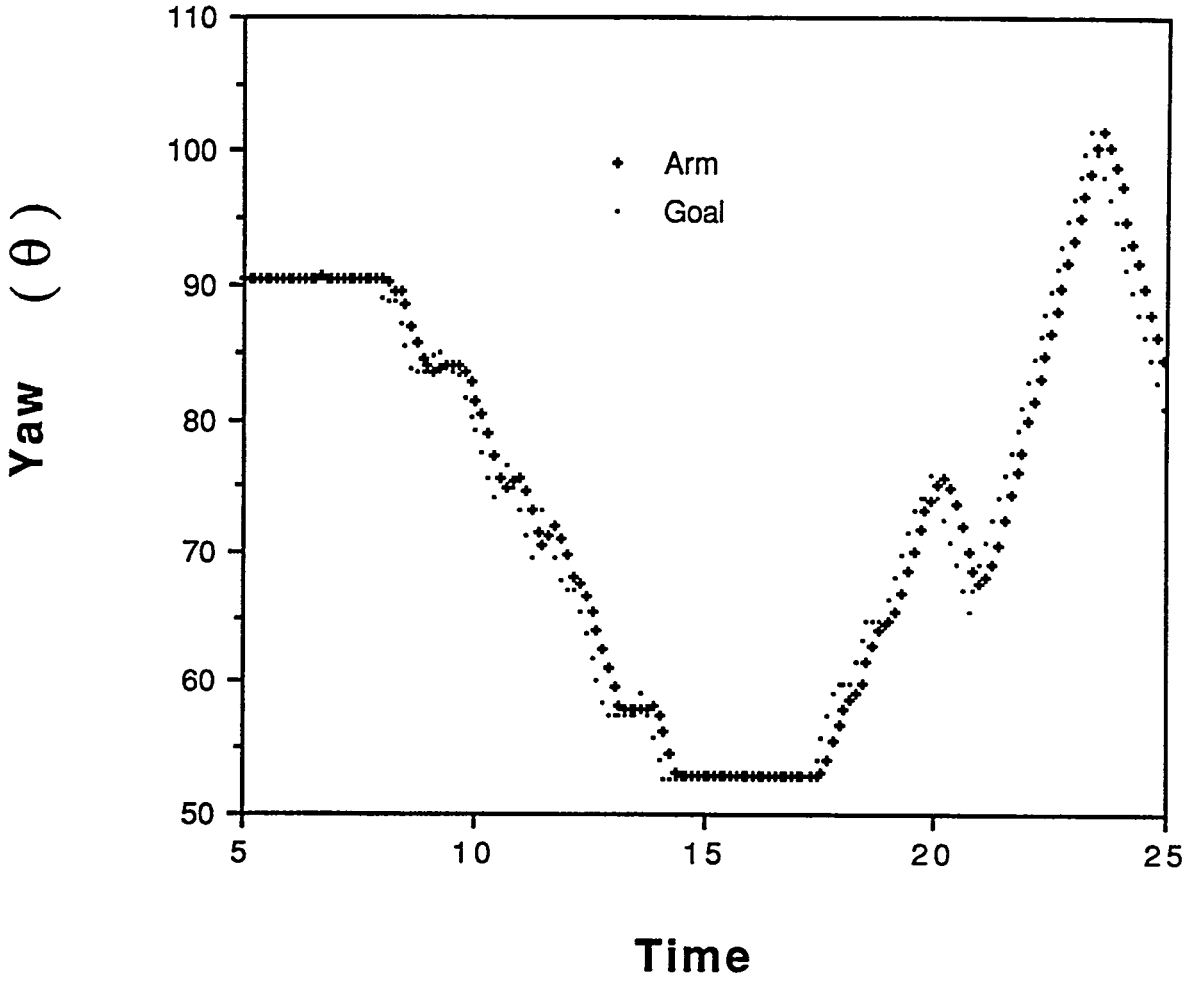

Fig. 11. Target and measured values for the yaw angle for the second experiment. The units are degrees.

3.3. BARREL RADIUS

The data in Fig. 10 lie on an arc of a circle. We can perform a least squares fit of the equation for a circle to the data and determine the center and radius of the circle. We estimated the radii for two sets of data (the data in Fig. 10 and another data set collected the same day). The estimated results were: 172 mm and 168 mm. These values are much smaller than the measured radius of the barrel: 290 mm.

At the start of an experiment, the vehicle is not moving and the arm makes a small sweep (70 mm to right and 70 mm to left) to determine the initial position and orientation for the arm. The estimated values of the radii for two sets of data from the initial arm

sweep were: 243 mm and 242 mm. Thus, the errors were much smaller for the data that were collected by a pure arm motion (without vehicle motion).

We decided to collect data for a pure vehicle motion (without arm motion). We defined a path for the vehicle that was approximately an arc of a circle about the center of the barrel. We collected three data sets (the first two data sets lost contact with the barrel in the middle of the experiment). The three estimates of the radii were very small: 66 mm, 80 mm, and 89 mm.

We concluded that the arm cannot be the source of errors and that we needed to investigate how vehicle motion causes errors in the calculation of the world coordinates of the measured surface. The details of our investigations are presented in Appendix B. We performed experiments in which we made a single pass from an initial position to a final position (for the normal experiments, the vehicle moves from an initial position to an intermediate position and then returns to the initial position). We measured the orientation of the vehicle at the initial and final positions. We found an orientation error of about 7 degrees.

In Appendix B, we will estimate the position of the vehicle during the experiment. Our results are summarized in Fig. 12. There are four curves in Fig. 12. The Vehicle Data curve is a plot of the position of the vehicle during the experiment as calculated by the vehicle reckoning system. The Barrel Data curve is the surface of the barrel during the experiment based on Eqs. (6) and (7). The Vehicle Calc curve is our estimate of the path of the vehicle during the experiment. The Barrel Calc curve is our estimate of the arc of the barrel that was measured by the range finder during the experiment.

Both of the two vehicle curves start at the same point and the two barrel curves start at the same point. There are substantial differences in both position and orientation of the vehicle at the end of the two vehicle curves. Consequently, there are major differences in the shapes of the two barrel curves (the Barrel Data curve has a radius of 98 mm, while the Barrel Calc curve has a radius of 290 mm). The vector from the end of the Vehicle Data curve to the end of the Barrel Data curve has about the same length as the vector from the end of the Vehicle Calc curve to the end of the Barrel Calc curve (1.680 m vs 1.686 m). However, there is a substantial difference (11.8 degrees) between the orientation of the two vectors (47.5 degrees vs 59.3 degrees).

3.4. REDUCTION OF DISTANCE ERROR

In this subsection, we will explore methods for reducing the low frequency errors observed in the distance measurements (see Fig. 5). In the last subsection and in Appendix B, we found that there are substantial errors in position and orientation for the vehicle. Consequently, our estimates of the surface normal are not correct. When we calculate the goal for the hand [see Eqs. (11) and (12)], the angle θ_c is incorrect. However, an incorrect value for θ_c should not cause an error in distance (the calculation is valid for arbitrary values of θ_c). The distance errors must be caused by errors in the position and orientation of the arm.

We have developed an error model for the arm. Choose a coordinate system with the x axis in the desired orientation (θ_c). Let e_x and e_y be the x and y components of the position error, θ_e be the orientation error, and D_e be the distance error:

$$e_x = (\mathrm{D_g} + \mathrm{L} + D_e)\cos\theta_e - (\mathrm{D_g} + \mathrm{L}) \tag{13}$$

$$e_y = (\mathrm{D_g} + \mathrm{L} + D_e)\sin\theta_e \tag{14}$$

The maximum error in Fig. 5 is about 25 mm. We assume that $D_e = 25$ mm. For our experiment, the value of $\mathrm{D_g} + \mathrm{L}$ is 164 mm. In Table 1, we display values of the position error for several values of the orientation error. As the orientation error increases, the x component of the position error decreases while the y component increases. We conjecture that we would have noticed the large errors in position and orientation at the bottom of Table 1. Thus, we speculate that the errors are in the range of the first two rows of the table. We plan future experiments to determine the errors in the position and orientation of the arm.

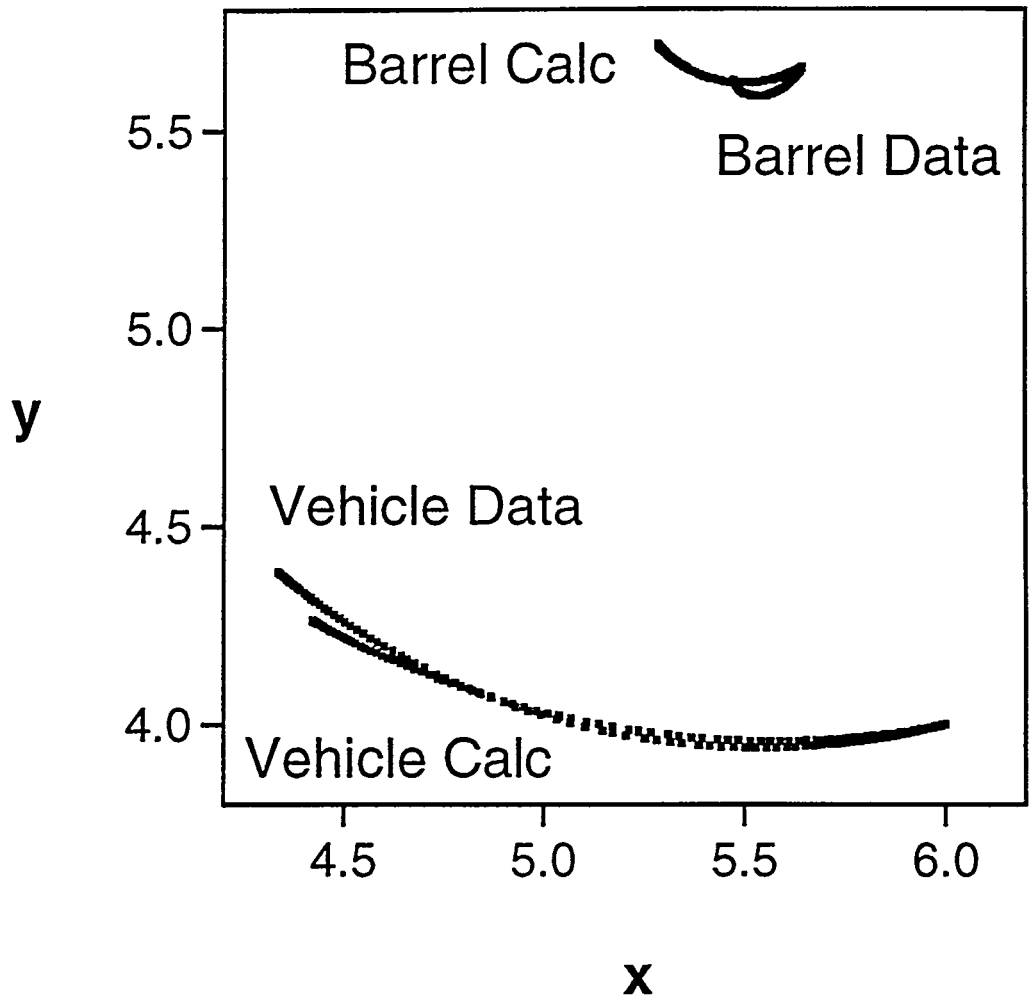

Fig. 12. Experimental and calculated data for the vehicle path and the barrel surface. The units of x and y are meters.

Table 1. Calculated values of the position error (e_x and e_y) for several values of the orientation error (θ_e).

Θ_e (Degrees)	e_x (mm)	e_y (mm)
0	25	0
7	24	23
15	19	49
30	0	94

We have used two methods to reduce the distance errors. The first is to modify the distance term $(D_g + L)$ in Eqs. (11) and (12):

$$x_c = x_d - (D_g + L + \Delta)\cos\theta_c \tag{15}$$

$$y_c = y_d - (D_g + L + \Delta)\sin\theta_c \tag{16}$$

where Δ is a correction term that depends on the distance error. The second method is to directly adjust the goal for the hand:

$$(x_c)_{n+1} = (x_c)_n + \Gamma\cos\theta_c \tag{17}$$

$$(y_c)_{n+1} = (y_c)_n + \Gamma\sin\theta_c \tag{18}$$

where Γ is a correction term that depends on the distance error. Although we implemented both methods, we will focus our attention on the first method in this subsection.

For each distance measurement (D_n), we can calculate the error (e_n):

$$e_n = D_n - D_g \tag{19}$$

Let u_n be the cumulative error:

$$u_{n+1} = u_n + e_n \tag{20}$$

We use a PI (proportional integral) model for the correction term (Δ_n):

$$\Delta_n = \rho\, e_n + \gamma\, u_n \tag{21}$$

The correction term does not depend on the most recent estimate of the cumulative error (u_{n+1}) because the most recent estimate depends on the most recent estimate of the error [which is the first term in Eq. (21)].

To develop an error model, we assume that the measured value for the yaw angle (θ_h) is equal to the target value (θ_c). [This assumption is supported by the experimental

data (see Fig. 7)]. To simplify the notation, we assume that the yaw angle is zero and develop an error model in the x direction. If $\theta_h = 0$, Eq. (4) becomes:

$$x_d = x_h + D + L \tag{22}$$

Thus, the next distance measurement (D_{n+1}) is given by:

$$D_{n+1} = (x_d)_{n+1} - (x_h)_{n+1} - L \tag{23}$$

If $\theta_c = 0$, Eq. (15) becomes:

$$x_c = x_d - (D_g + L + \Delta) \tag{24}$$

If we assume that the arm reaches its goal [$(x_h)_{n+1} = (x_c)_n$]:

$$(x_h)_{n+1} = (x_d)_n - (D_g + L + \Delta_n) \tag{25}$$

Using Eqs. (23) and (25), we derive the following error model:

$$e_{n+1} = (x_d)_{n+1} - (x_d)_n + \Delta_n \tag{26}$$

Using Eq. (21) and neglecting the disturbance term [$(x_d)_{n+1} - (x_d)_n$], the error model becomes:

$$e_{n+1} = \rho\ e_n + \gamma\ u_n \tag{27}$$

The error model is a linear second order system with constant coefficients. Stability requires that the magnitude of the eigenvalues be less than unity.

To determine the eigenvalues (k), we assume that the cumulative error is growing exponentially:

$$u_n = k^n u_0 \tag{28}$$

Using Eq. (20):

$$e_n = (k-1)u_n \tag{29}$$

Using Eq. (29):

$$e_{n+1} = (k-1)k\,u_n \tag{30}$$

Using Eqs. (27) to (30), the characteristic equation for the eigenvalues is:

$$(k-1)k = \rho\,(k-1) + \gamma \tag{31}$$

The eigenvalues satisfy:

$$k = (1/2)\,[(1+\rho) \pm \sqrt{(1+\rho)^2 - 4\,(\rho - \gamma)}\,] \tag{32}$$

We have chosen the parameters so that the eigenvalues are critically damped:

$$\gamma = -(1/4)\,(1-\rho)^2 \tag{33}$$

$$k = (1+\rho)/2 \tag{34}$$

If the magnitude of the eigenvalue k is less than unity, ρ must be in the range from -3 to 1. As ρ decreases from 1 to -3, γ decreases from 0 to -4. We performed experiments for values of ρ that ranged from 0.3 to -0.3 (see Table 2). As the parameter ρ decreased, the magnitude of the eigenvalue k decreased and the measured distance from the range finder to the surface began to oscillate. To reduce the oscillations, we selected the parameter values on the top row of Table 2.

Table 2. Values of the eigenvalue k and the parameter γ for several values of the parameter ρ.

ρ	γ	k
0.3	–0.12	0.65
0.1	–0.20	0.55
–0.1	–0.30	0.45
–0.3	–0.42	0.35

We will conclude this section by discussing three experiments in which we used the correction term to reduce the distance error. We will call the experiments: 3.1, 3.2, and 3.3. The distance measurements for the three experiments are presented in Figs. 13, 14, and 15. In Fig. 5, the maximum error is about 25 mm. In Fig. 13, the errors are less than 10 mm except for a transition at about 10 seconds [the goal (D_g) is shown as a dotted line]. In Fig. 14, most of the errors are less than 10 mm and all of the errors are less than 15 mm. In Fig. 15. the errors are less than 10 mm except for a transition at about 10 seconds until the errors become very large after 22 seconds.

In Fig. 5, the errors change slowly (they are negative from 6 sec. to 18 sec. and then become positive). In Figs. 13 to 15, the correction term causes the errors to oscillate rapidly in sign and magnitude. Thus, the correction term is capable of changing the sign of the distance error. We are disappointed that the correction term is not more successful at reducing the magnitudes of the errors. In the remainder of this section, we will explore why the correction term is not more succesful in reducing the errors.

Figures 16 to 18 display the correction term (Δ) for the three experiments. The shape of the correction term is approximately the same for the three experiments. For the first seven seconds the correction is positive. In the neighborhood of 10 sec., the

correction term is negative with fluctuations in magnitude. After 13 sec., the correction term is generally positive (with fluctuations in magnitude in Figs. 17 and 18).

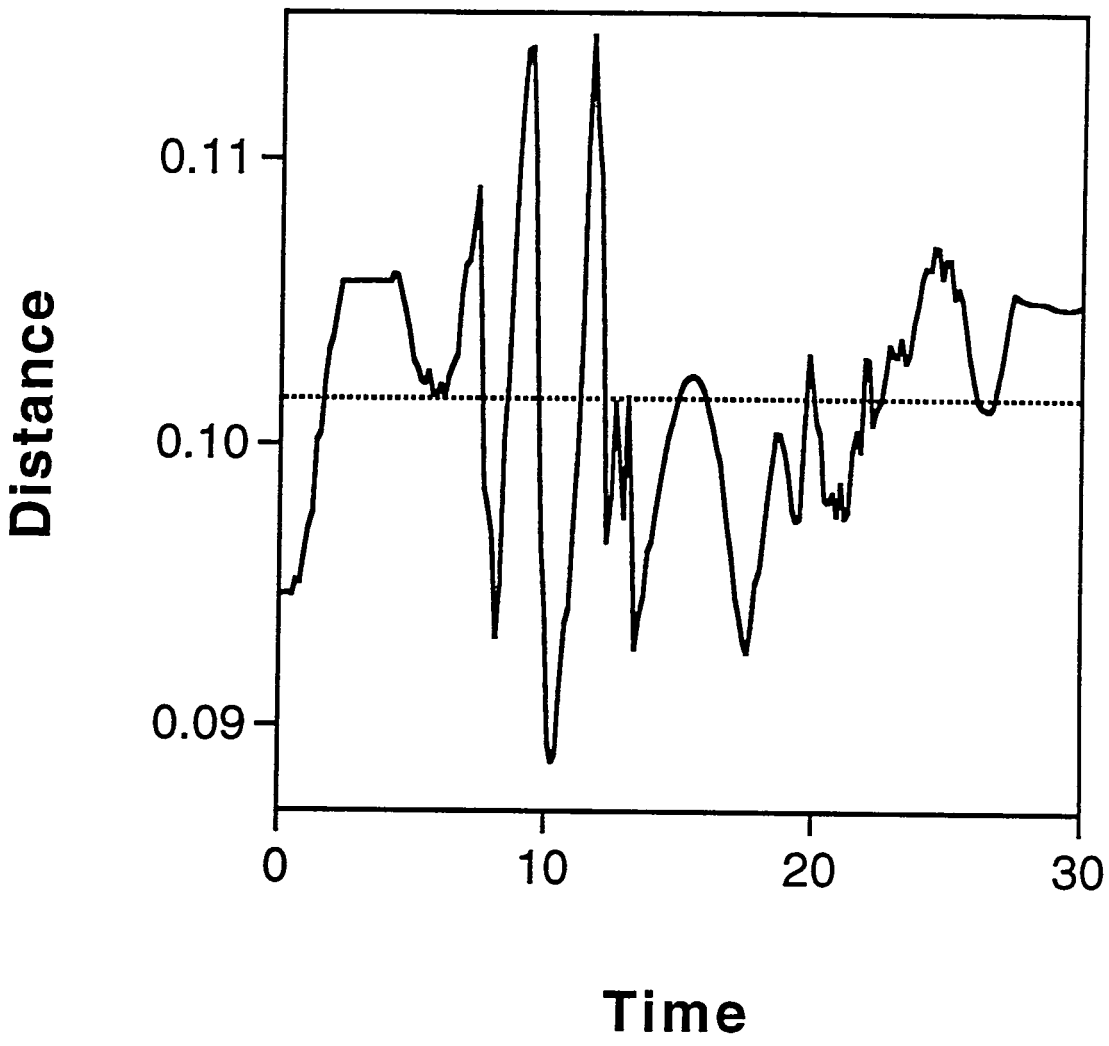

Fig. 13. The distance from the range finder sensor to the unknown surface for Experiment 3.1. The units are meters.

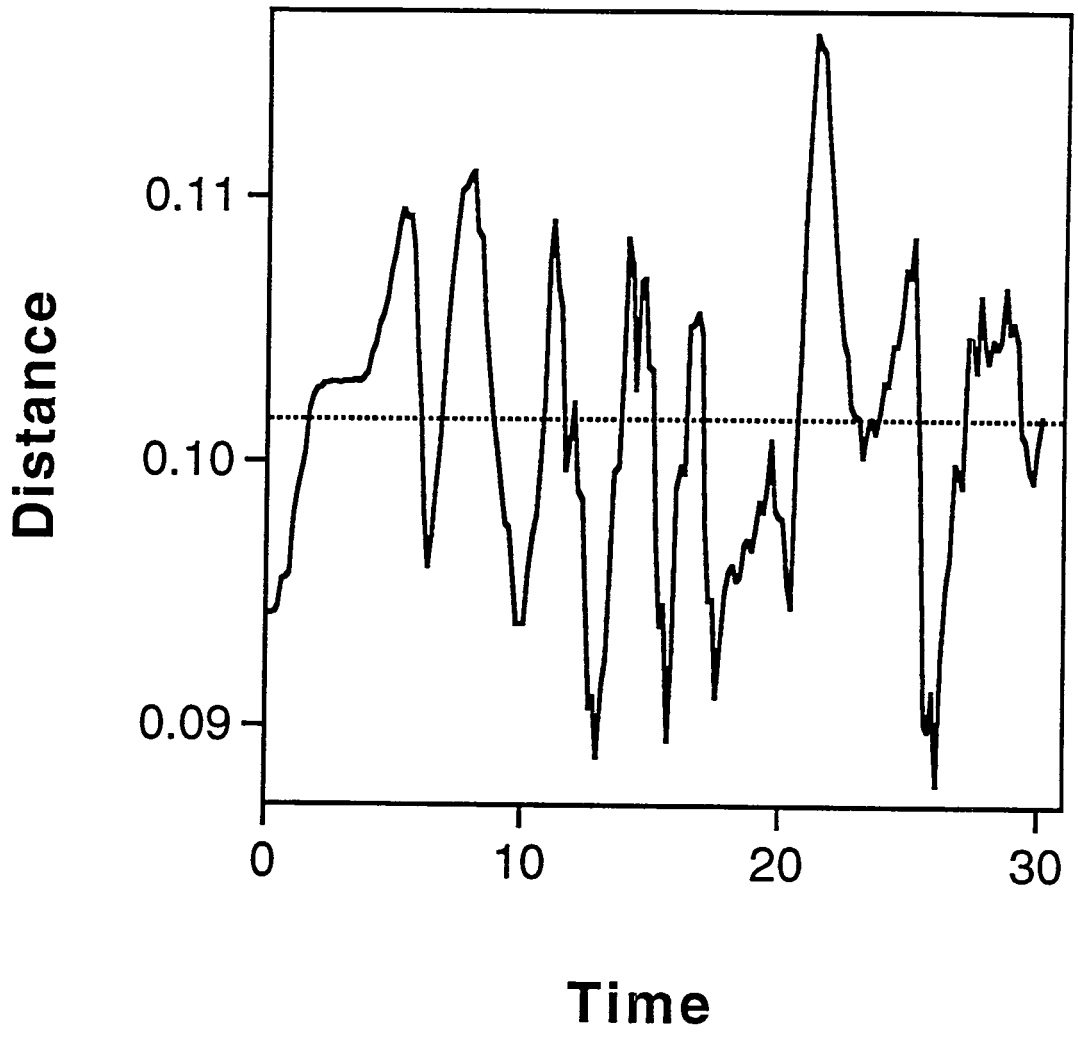

Fig. 14. The distance from the range finder sensor to the unknown surface for Experiment 3.2. The units are meters.

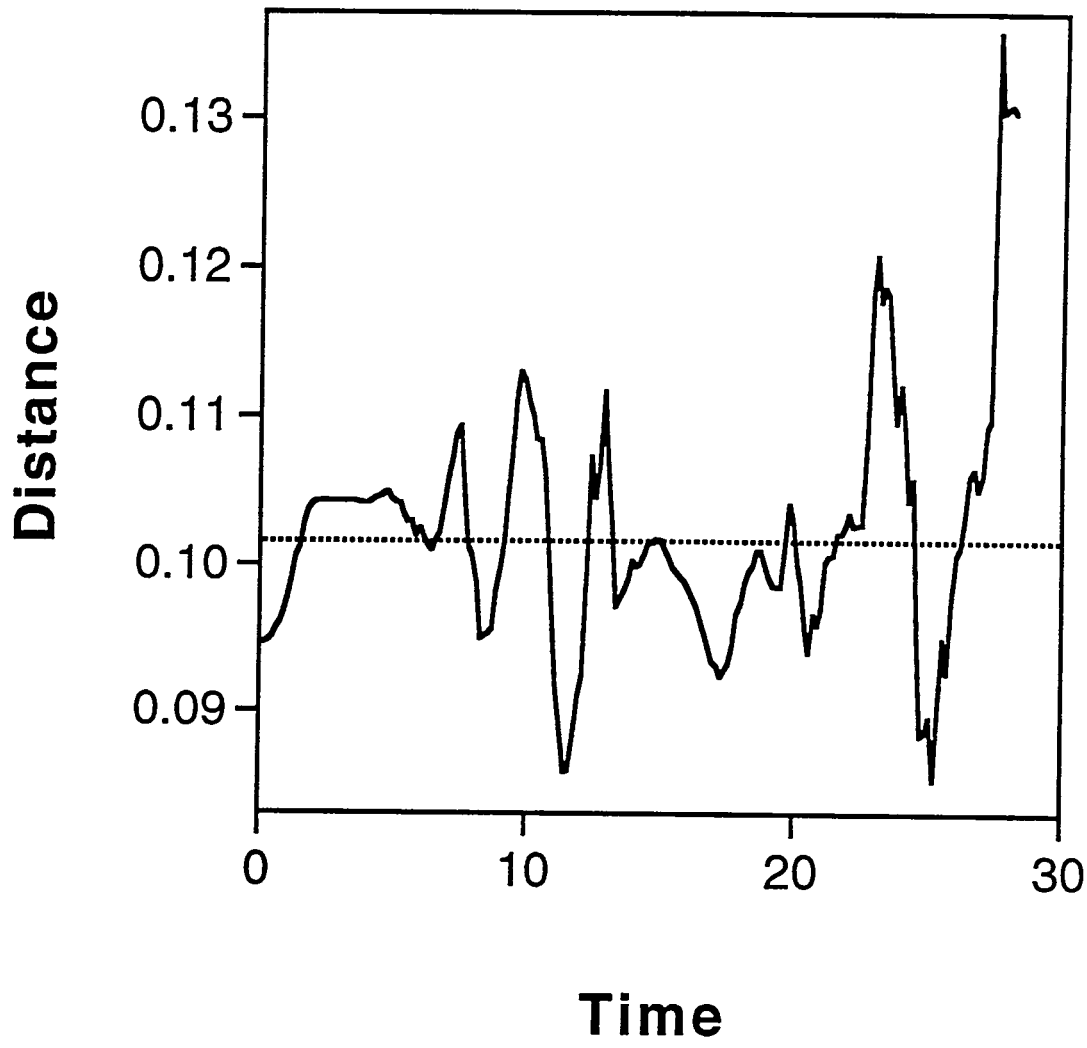

Fig. 15. The distance from the range finder sensor to the unknown surface for Experiment 3.3. The units are meters.

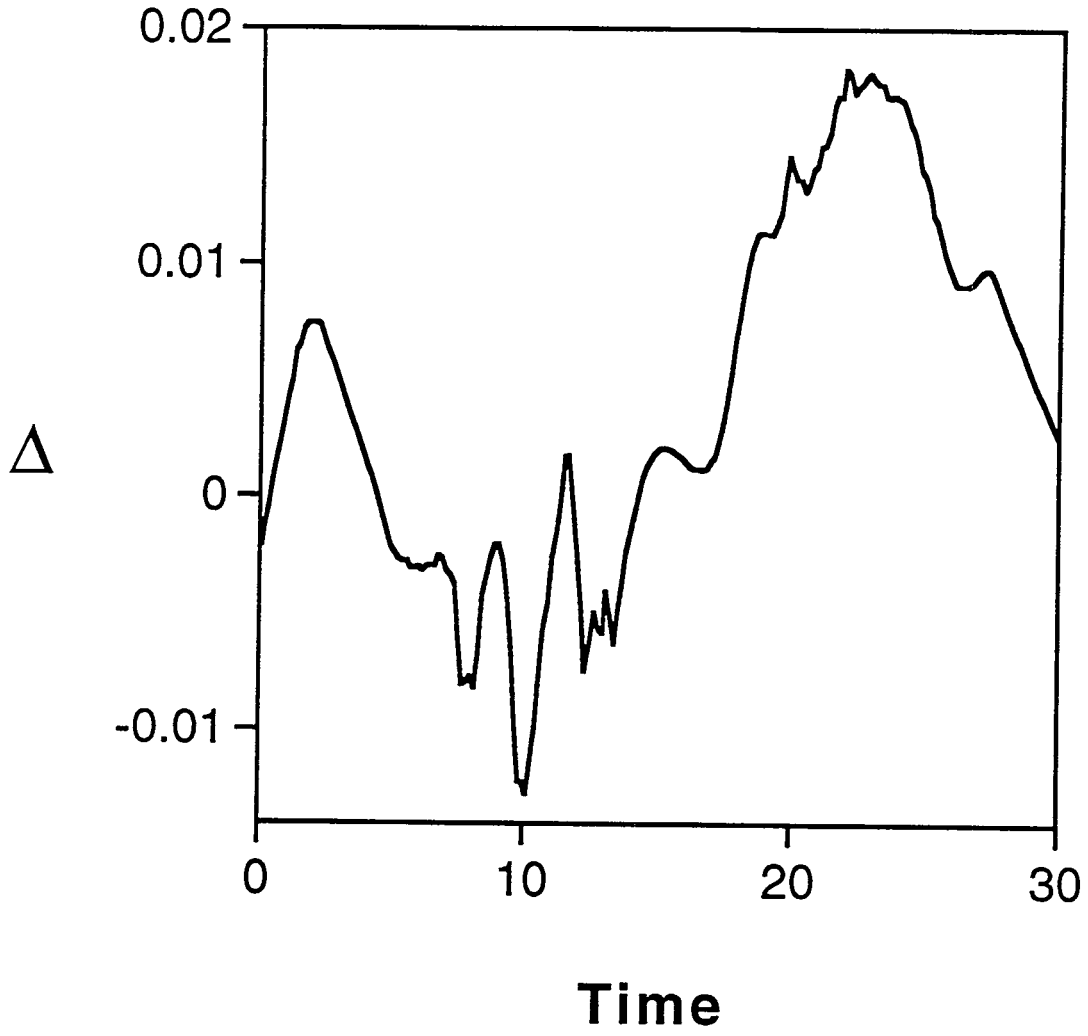

Fig. 16. The calculated values for the correction term for Experiment 3.1. The units are meters.

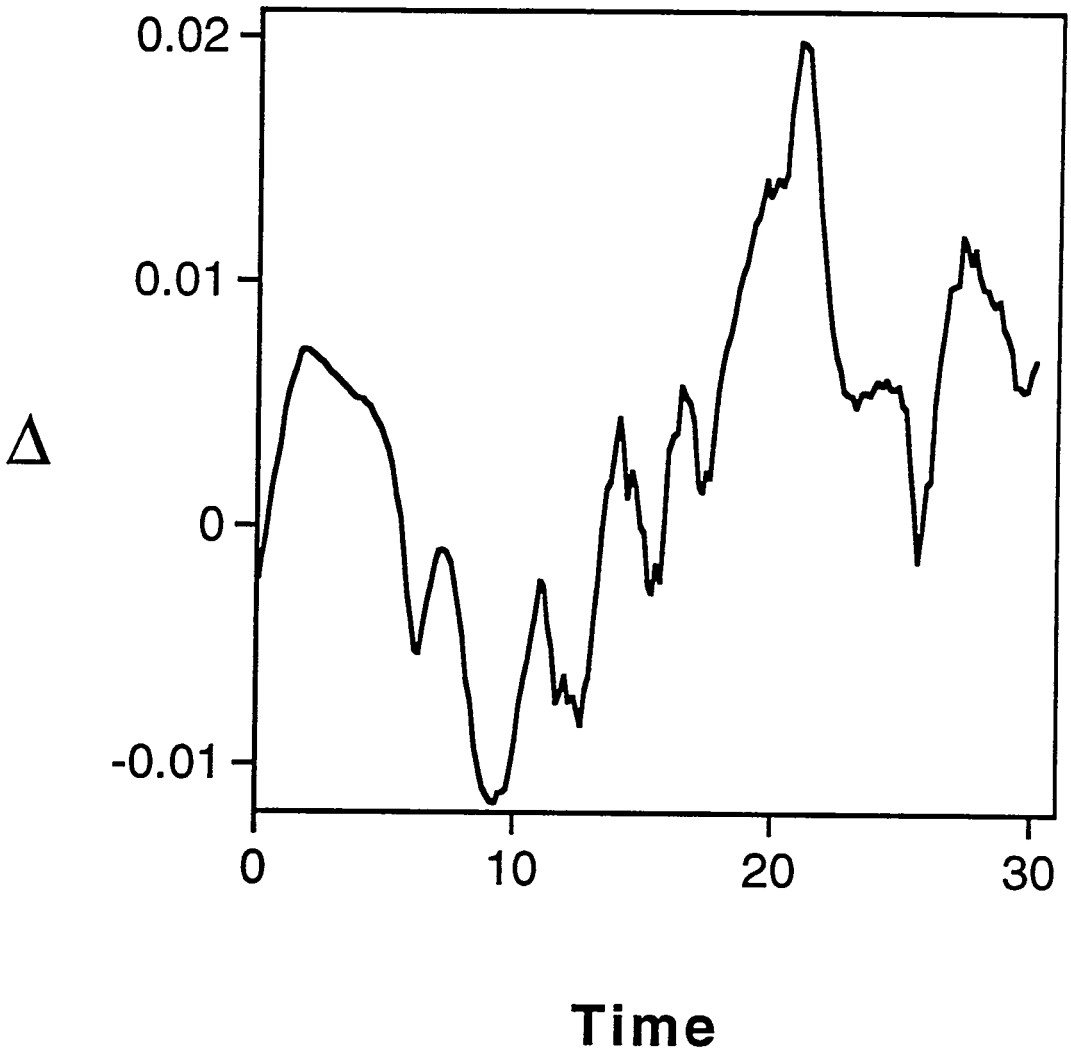

Fig. 17. The calculated values for the correction term for Experiment 3.2. The units are meters.

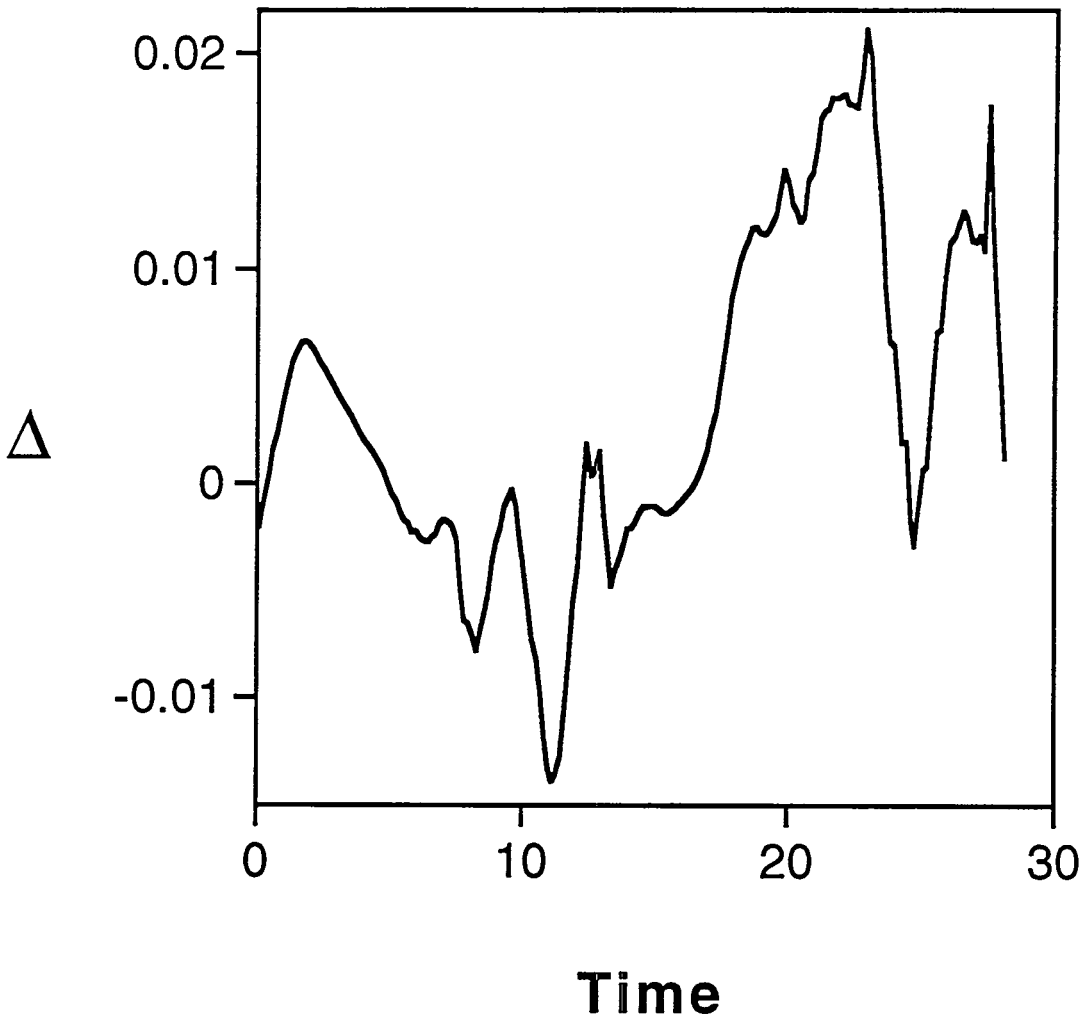

Fig. 18. The calculated values for the correction term for Experiment 3.3. The units are meters.

The measured values of the yaw angle are plotted in Figs. 19 to 21 for the three experiments. For Experiment 3.1 (Fig. 19), the yaw angle starts at 90 degrees. In the neighborhood of 10 seconds, the angle makes a rapid transition to about 63 degrees and remains at that orientation for the rest of the experiment. Thus, the largest distance errors (Fig. 13) and the rapid fluctuations in the correction term (Fig. 16) are associated with rapid changes in the yaw angle.

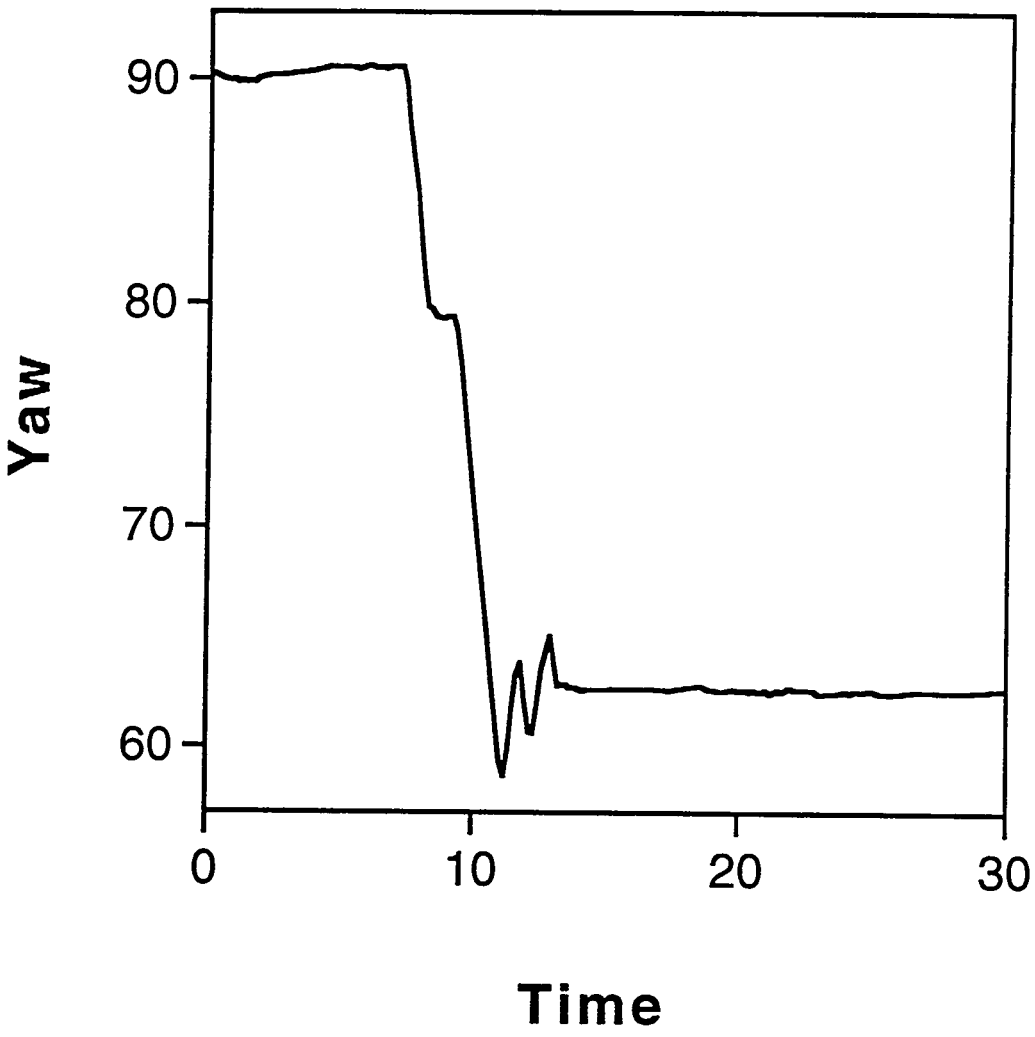

Fig. 19. The measured values for the yaw angle for Experiment 3.1. The units are degrees.

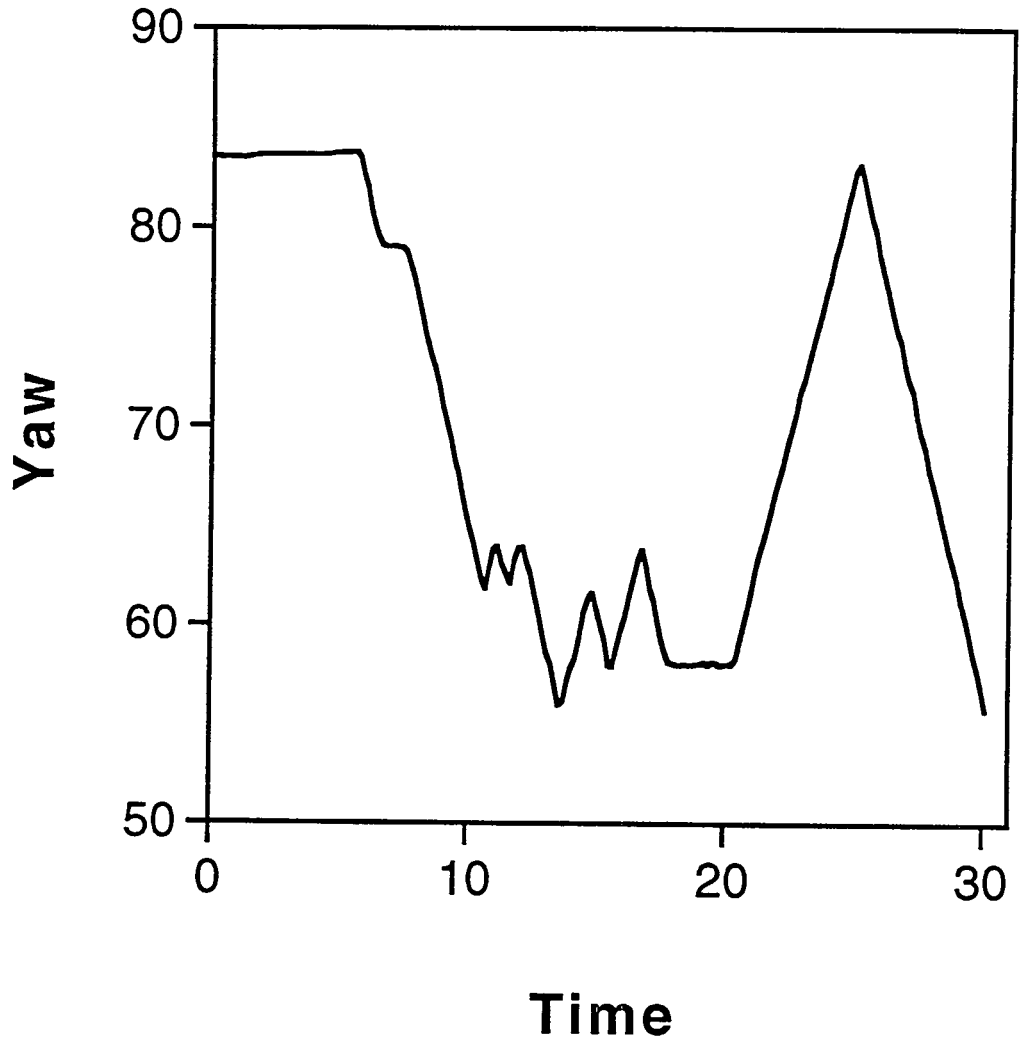

Fig. 20. The measured values for the yaw angle for Experiment 3.2. The units are degrees.

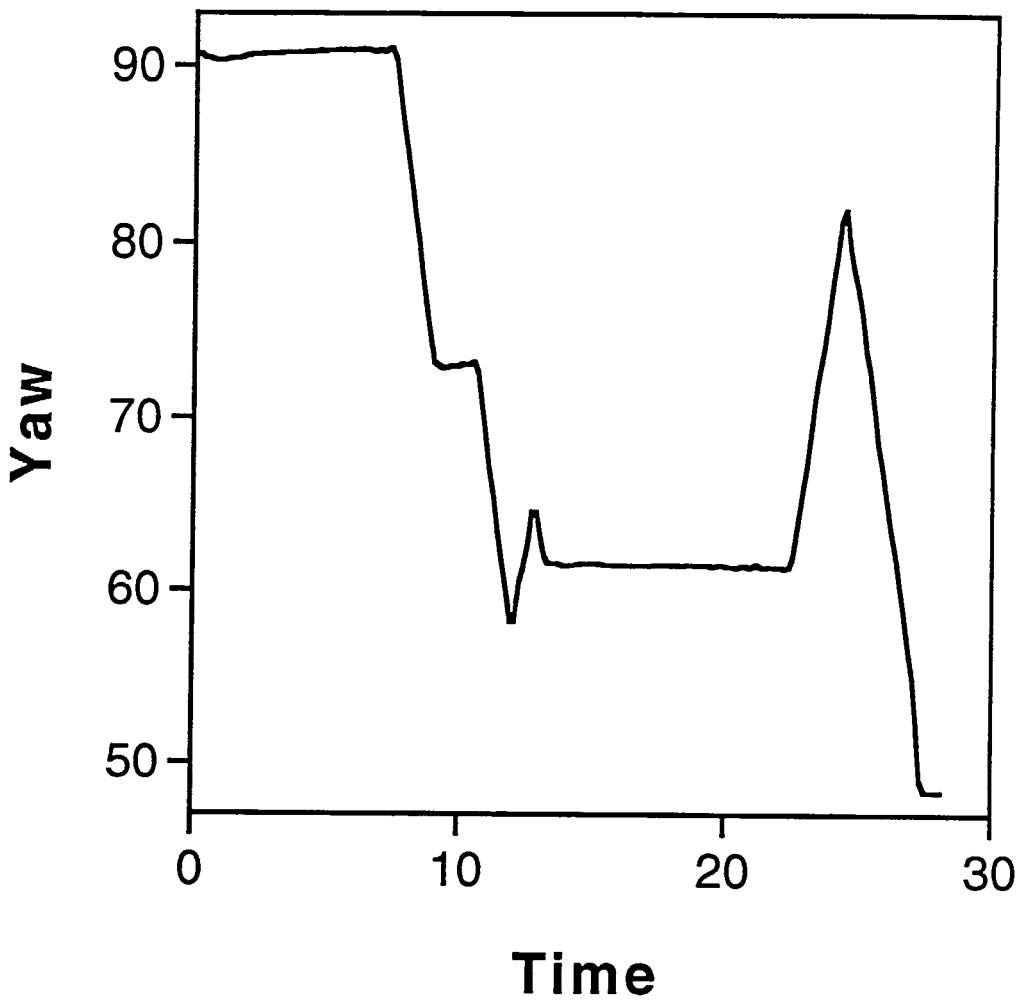

Fig. 21. The measured values for the yaw angle for Experiment 3.3. The units are degrees.

For Experiment 3.2 (Fig. 20), the yaw angle is 84 degrees for the first 6 seconds, drops to 62 degrees by 11 sec., and fluctuates from 11 to 18 seconds. From 20 to 30 sec., the angle rapidly climbs from 58 degrees to 83 degrees and then rapidly drops to 52 degrees. All of the rapid fluctuations in the correction term (Fig. 17) are associated with rapid changes in the yaw angle. During Experiment 3.3 (Fig. 21), the yaw angle does not fluctuate during the period from 13 to 22 seconds and the correction term (Fig. 18) does not have rapid oscillations during this period.

The calculated positions of the surface of the barrel (in world coordinates) are displayed in Figs. 22 to 24 for the three experiments. During the experiments, the vehicle follows a circular path in a clockwise direction and returns to the initial location. In Fig. 10, the calculated positions during the clockwise sweep coincide with the values during the counterclockwise sweep. In Figs. 22 to 24, the curves leading from the start positions are not consistent with the curves returning to the end positions.

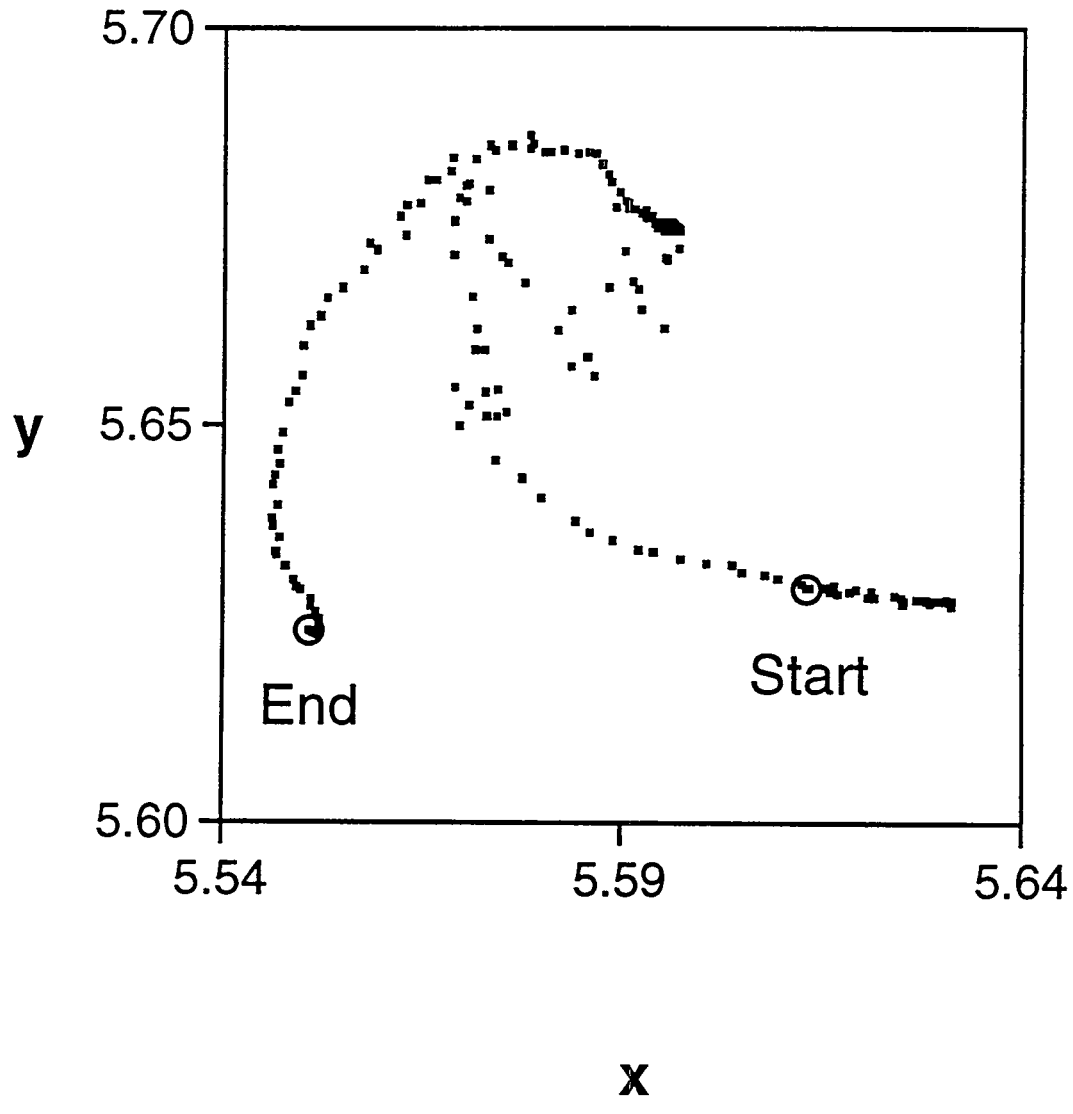

Fig. 22. The calculated position of the unknown surface in the world coordinate system for Experiment 3.1. The units of x and y are meters.

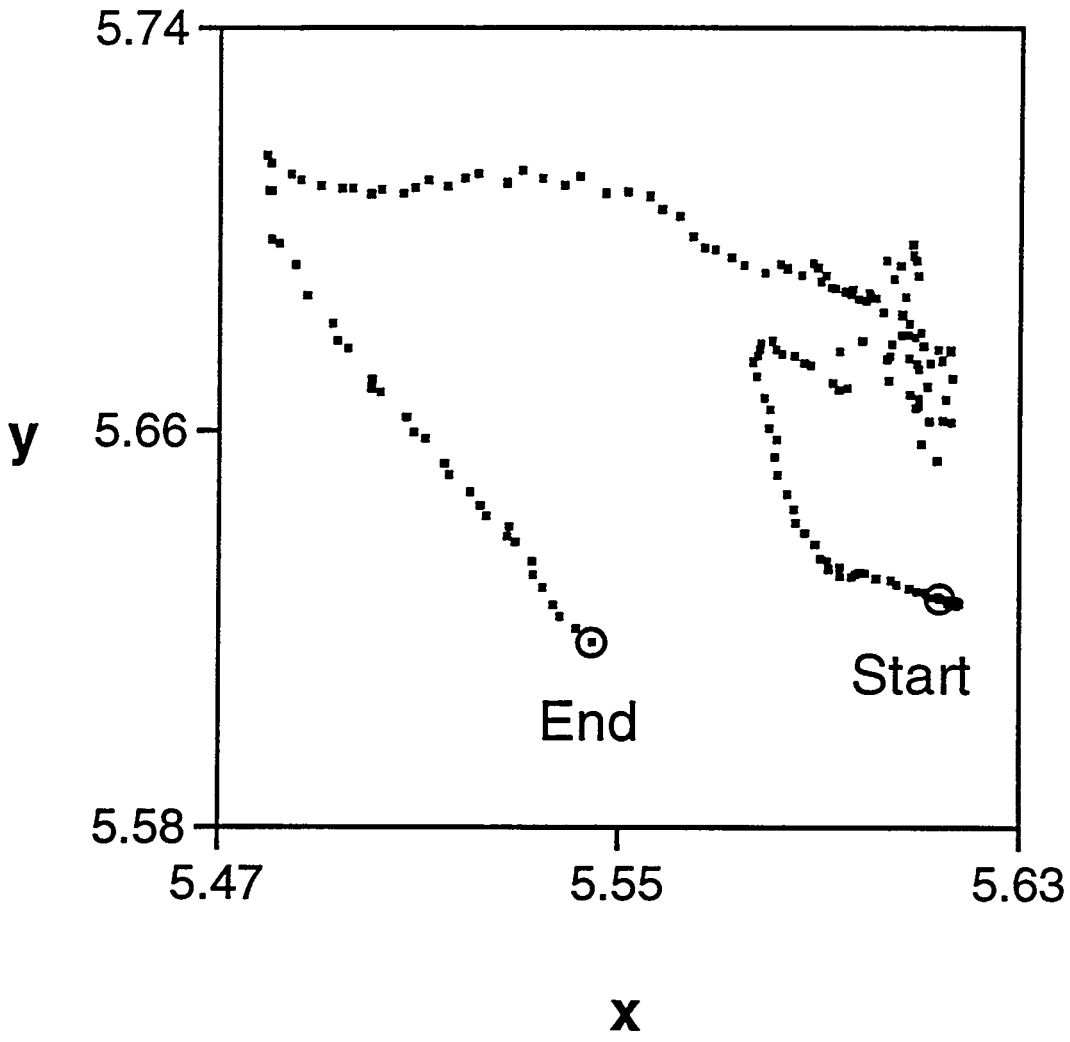

Fig. 23. The calculated position of the unknown surface in the world coordinate system for Experiment 3.2. The units of x and y are meters.

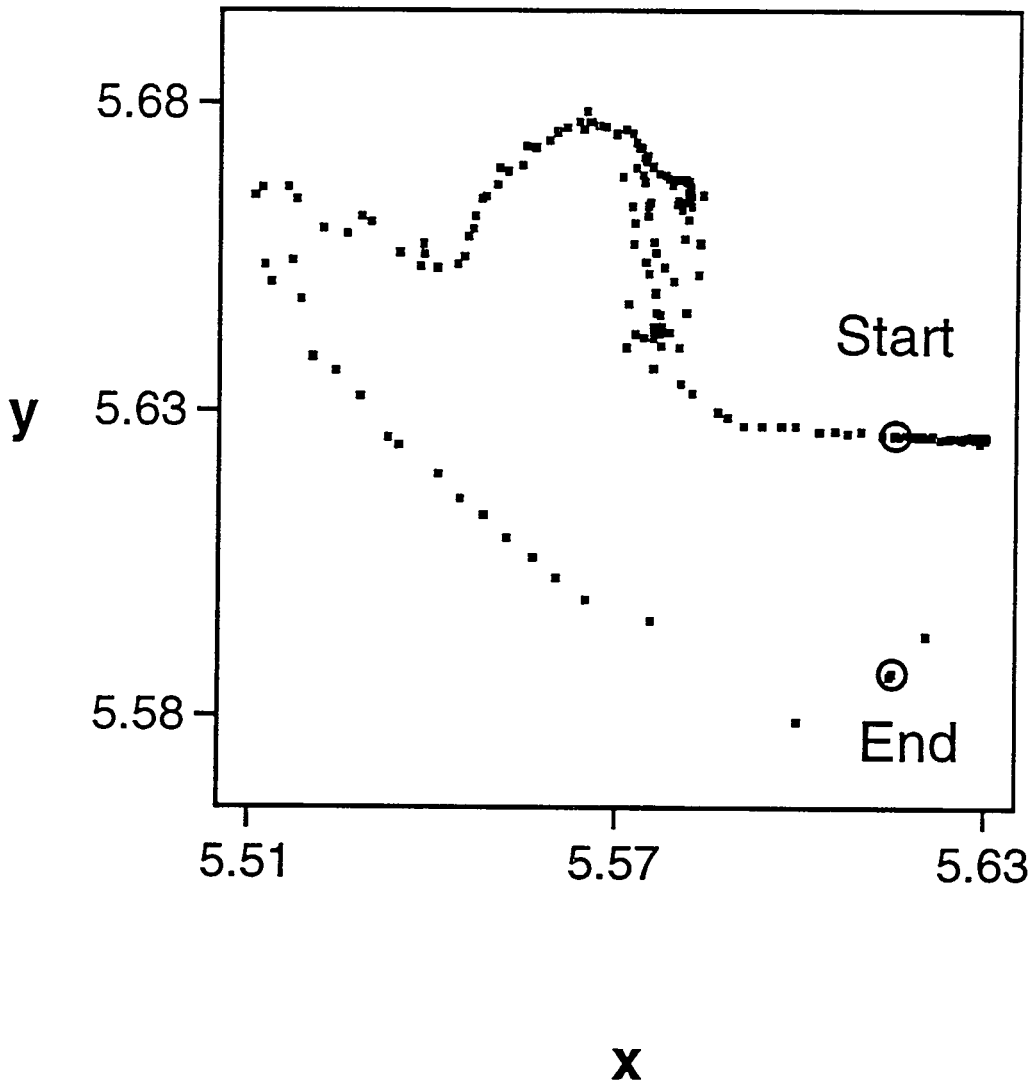

Fig. 24. The calculated position of the unknown surface in the world coordinate system for Experiment 3.3. The units of x and y are meters.

During Experiment 3.1 (Fig. 22), the yaw angle has two values and both the initial data and the final data lie on an arc (the initial arc has a much larger radius than the final arc). During the transition from the inital value (90 degrees) to the final value (63 degrees), the data are scattered and do not lie on an arc.

For the three experiments, the range in the calculated values of the surface of the barrel is much less than expected. In Fig. 10, the range in y values is about 200 mm. Furthermore, in the last subsection and in Appendix B, we demonstrated that the radii for

the calculated values were much less than the measured radius of the barrel (290 mm). In Fig. 22, the arc that leads to the final value appears to have a length of about 180 degrees. For the barrel, the length of the chord that joins the ends of a 180 degree arc would be 580 mm. Since the range in the values that define the boundary of Fig. 22 is 100 mm for both x and y, the figure cannot display a feature that is 580 mm long.

Without arm motion, the radius of the calculated surface of the barrel can be very small (see Appendix B). When the arm moves, the calculated surface of the barrel can be quite close to the measured radius. In Figs. 22 to 24, we observe both regions of high curvature (small radius) and regions of low curvature (large radius).

We will not be able to attain the goals of the experiment (small distance errors and the sensor normal to the surface) until we have accurate calculated positions for the surface of the unknown object.

4. CONCLUDING REMARKS

We have discussed four series of surface following experiments using a range finder mounted on the end of an arm that is mounted on a vehicle. The goal is to keep the range finder at a fixed distance from an unknown surface and to keep the orientation of range finder perpendicular to the surface.

Our results demonstrate the importance of experimental robotics. All of our calculations worked in simulation. To calculate points on the surface of an object, we require data from three systems: a range detector, an arm, and a vehicle. The errors and uncertainties that exist in each of these systems can propagate and accumulate in unexpected ways. For the first series of experiments, we naively assumed that calculations that worked in simulation would work with experimental data. When we obtained unexpected results and faced with a demonstration deadline, we introduced parameters (a filter for the surface normal and a velocity bound for the yaw angle) that enabled the experiment to be performed for a variety of concave and convex surfaces.

For the second (and subsequent) series of experiments, we identified problems, collected detailed data on the problems, identified reasons for the problem, and (if possible) revised our methods to overcome the problems. The first problem was the scatter in the surface normal data (see Fig. 3). We collected data (Fig. 8), revised our method of calculation (did not average data, fit line through more data points, used overlapping data sets, and did not calculate the normal unless there was sufficient spread in the data), and obtained the results in Fig. 9.

The second problem was that the radius of the calculated surface was significantly different than the measured radius of the barrel. We performed a series of experiments with the arm in a fixed position and determined that the position and orientation errors in the dead reckoning system for the vehicle were the source of the radii errors.

The third problem was that the measured distance to the unknown surface had errors that were systematic, low frequency, and had magnitudes up to 25 mm. Although we introduced a correction term, we were unable to significantly reduce the distance errors. The distance errors must be caused by errors in the forward kinematics calculations that estimate the position and orientation of the arm.

Our fundamental conclusion is that we must redesign the experiment. We need to validate the forward kinematics calculations for the arm. To eliminate the radii errors, we can either improve the self location system for the vehicle or adopt a strategy of moving the arm more to obtain a better estimate of the unknown surface.

5. ACKNOWLEDGMENT

This research was performed under sponsorship of the Engineering Research Program, Office of Basic Energy Sciences, of the U.S. Department of Energy, under contract DE-AC05-84OR21400 with Martin Marietta Energy Systems, Inc.

REFERENCES

[1] F. G. Pin et al., "Autonomous Mobile Robot Research Using the HERMIES-III Robot," Proceedings of the IEEE RSJ International Workshop on Intelligent Robots and Systems, IROS '89, September 4--6, 1989, Tsukuba, Japan, 251-256.

[2] D. B. Reister, "A New Wheel Control System for the Omnidirectional HERMIES-III Robot," *Robotica* **10**, 351-360 (1992).

[3] J. P. Jones et al., "Hetero Helix: Synchronous and Asynchronous Control Systems in Heterogeneous Distributed Networks," *Robotics and Autonomous Systems* **10** 85-99 (1992).

[4] M. A. Unseren, "Input Relegation Control for Gross Motion of a Kinematically Redundant Manipulator," Oak Ridge National Laboratory Technical Report No. ORNL/TM-12165, October 1992.

[5] J. E. Baker, "Empirical Characterization of a High Intensity Proximity Sensor," *Sensors* **10** 29-32 (1993).

[6] J. E. Baker, "Terrain Following and Mapping of Arbitrary Surfaces Using High Precision Proximity Data," *Optical Engineering* **32,** 1117-1124 (1993).

[7] D. B. Reister and M. A. Unseren, "Position and Constraint Force Control of a Vehicle with Two or More Steerable Drive Wheels," *IEEE Transactions on Robotics and Automation* **9**, 723-731 (1993).

APPENDIX A

RANGE FINDER EXPERIMENTS

The body of this paper discusses a surface following experiment by a mobile manipulator. The experiment requires the interaction of three systems: the arm, the vehicle, and the range finder. In this appendix, we discuss the behavior of one of the three interacting systems: the range finder. For another project, we used the range finder to measure the distance from HERMIES-III to the floor and observed unexpected discontinuities in the data. We performed a series of experiments to investigate the behavior of the range finder system. This appendix will discuss the results of our investigations.

Since HERMIES-III has smooth round wheels, we expect that the distance from the frame of the vehicle to the floor should vary continuously. However, the measured data were discontinuous (see Fig. 25). The initial portion of Fig. 25 is expanded in Fig. 26. In Fig. 26, the measured values have the following pattern: six values that are nearly constant followed by another group of six values. We performed a series of experiments to investigate this unexpected behavior.

The A to D (Analog to Digital) board produces 12 bit output (or 4096 values). The sensor produces an output signal between 0 and 10 volts where the distance range was from 0 to 203 milimeters (0 to 8 inches). The jumpers on the A to D board had been set incorrectly and the board was expecting values in the range from -10 and 10 volts. Thus, the maximum resolution was 8 inches/2048 = 0.004 inches = 0.1 millimeter. We reset the jumpers and doubled the resolution to 8 inches/4096 = 0.002 inches = 0.05 millimeter.

We found that we could read the A to D board 35 times in 0.01 seconds (at 3500 Hz). Our previous procedure was to read the board 10 times in 0.01 seconds and produce an average value. Now we read the board 4 times in 0.01 seconds and keep all of the data.

After increasing the resolution and keeping all of the data, the measured data on the distance from HERMIES-III to the floor are displayed in Figs. 27 and 28. Fig. 27 plots all of the data for a two second experiment, while Fig. 28 displays the data for 0.5 seconds during a rapid increase in distance. Four data points are plotted for each sampling period (at 100 Hz). Sometimes the four data points have a single value and sometimes there are four distinct values. The data values are integers and there are about 20 integers per millimeter.

The data in Fig. 28 has the same pattern as the data in Fig. 26: the data are in groups that are six sampling periods in duration. Although we do not know why the data have the pattern, we concluded that we could easily fit a line or curve to the data in Fig. 28.

We calibrated the range finder and found that the sensor is accurate between 64 millimeters and 152 millimeters (2.5 inches and 6 inches).

Our major conclusion is that we should carefully look at the detailed data that we collect during an experiment.

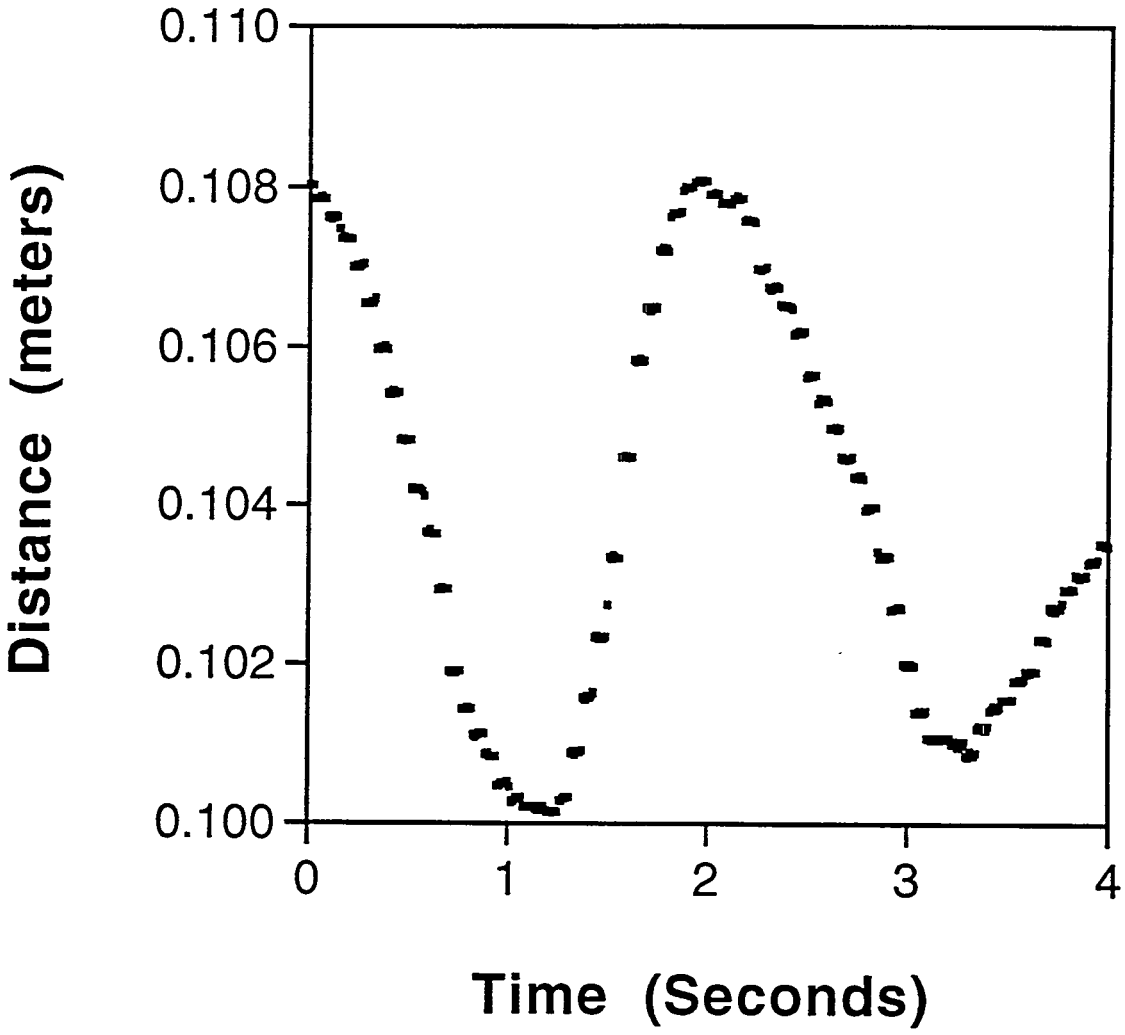

Fig. 25. Initial measurements of the distance from the HERMIES-III vehicle to the floor.

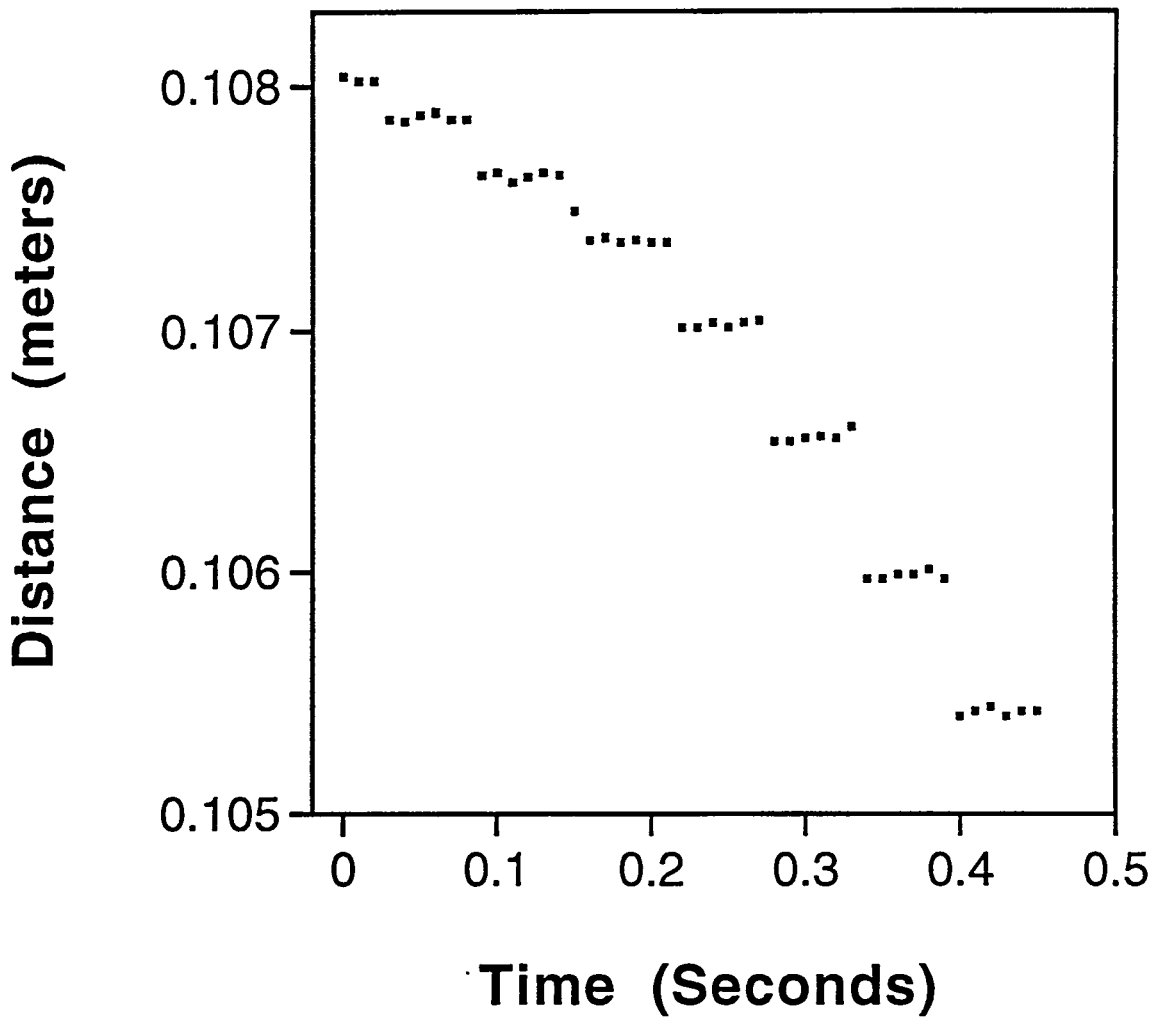

Fig. 26. Initial measurements of the distance from the HERMIES-III vehicle to the floor. Expanded time scale.

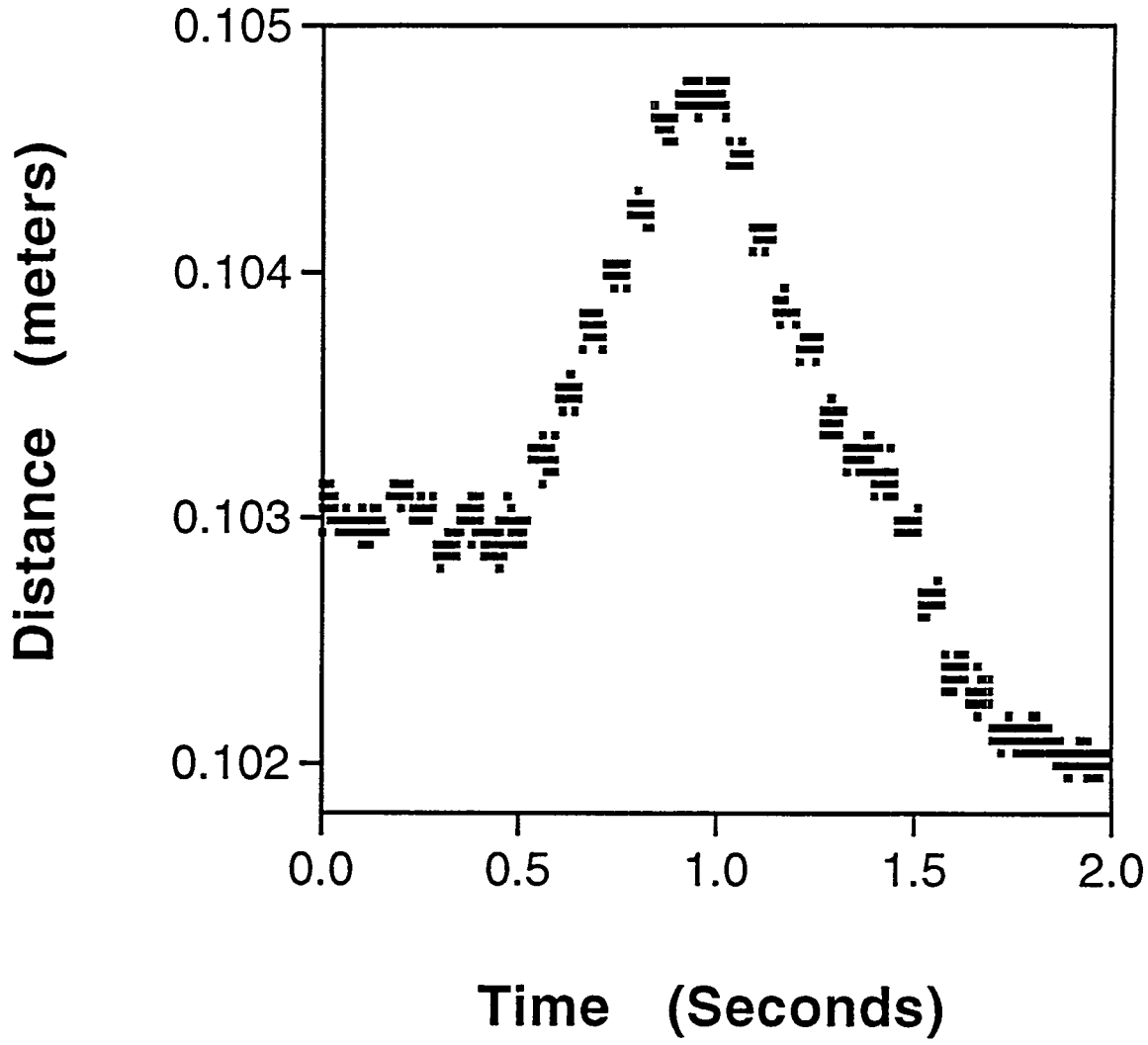

Fig. 27. Final measurements of the distance from the HERMIES-III vehicle to the floor.

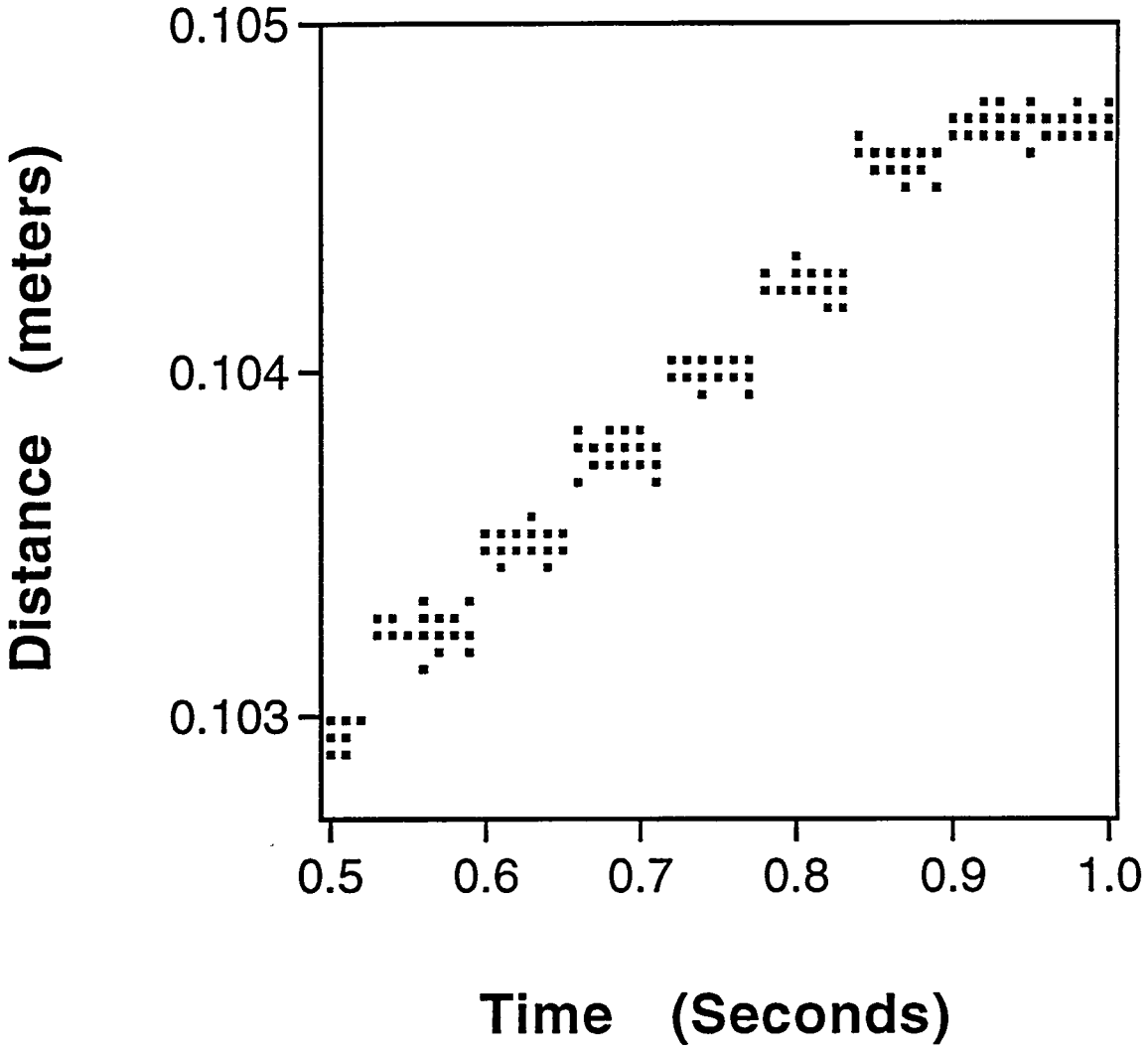

Fig. 28. Final measurements of the distance from the HERMIES-III vehicle to the floor. Expanded time scale.

APPENDIX B

EXPERIMENTS WITH VEHICLE MOTION AND WITHOUT ARM MOTION.

As discussed in Section 3.3, we decided to collect data for a pure vehicle motion (without arm motion). We defined a path for the vehicle that was approximately an arc of a circle about the center of the barrel. We collected three data sets. The three estimates of the radii were very small: 66 mm, 80 mm, and 89 mm (the barrel radius is 290 mm).

To identify the sources of the errors, we performed four experiments in which we made a single pass from an initial position to a final position (for the normal experiments, the vehicle moves from an initial position to an intermediate position and then returns to the initial position). We measured the orientation of the vehicle at the initial and final positions.

In this appendix, we will discuss the experimental data and we will develop a model that estimates the position and orientation of the vehicle during the experiment.

The data from the four single pass experiments are displayed in Table 3. The experiments alternated in the direction of motion. The measured values were obtained by measuring the initial and final orientations of the vehicle. The reckoned values are the change in orientation that was calculated by the vehicle. The four sets of data are consistent (all of the measured data is within 0.4% of the mean value).

Table 3. Change in Orientation for the Vehicle During the Four Single Pass Experiments. The Units are Degrees.

Case	Measured	Reckoned	Difference
1	–47.899	–54.717	6.818
2	+47.802	+54.720	6.918
3	–47.593	–54.518	6.925
4	+47.824	+54.517	6.693

We would like to estimate the position and orientation of the vehicle during the experiment. Our notation is defined in Fig. 29. The position and orientation of the vehicle are defined by world coordinates (x_p, y_p, ϕ_p). The arm does not move (in the platform coordinate system) during the experiment. The range finder measures the distance from the end of the arm to a point on the surface of the barrel with world coordinates (x_s, y_s). The angle of the line from the center of the barrel (x_0, y_0) to the surface point (x_s, y_s) is η in world coordinates (in Fig. 29, the angle is negative). The angle of the line from the surface point (x_s, y_s) to the center of the barrel (x_0, y_0) is σ in vehicle coordinates.

Given the angle η, the surface point is given by:

$$x_s = x_0 + R_b \cos \eta \tag{35}$$

$$y_s = y_0 + R_b \sin \eta \tag{36}$$

where R_b is the radius of the barrel (R_b = 290 mm). The angle η is determined by:

$$\eta = \phi_p + \sigma - p \tag{37}$$

Since the arm is in the home position, $(x_h, y_h) = (1.454, 0.365)$. Using Eqs. (4) and (5), the surface point in the vehicle coordinate system (x_d, y_d) is given by:

$$x_d = x_h + D + \mathrm{L} = 1.516\ \mathrm{m} + D \tag{38}$$

$$y_d = y_h = 0.365\ \mathrm{m} \tag{39}$$

Let (x_a, y_a) be the center of the barrel in the vehicle coordinate system:

$$x_a = x_d + R_b \cos\sigma \tag{40}$$

$$y_a = y_d + R_b \sin\sigma \tag{41}$$

The radius (R_p) from the center of the barrel to the vehicle is determined by:

$$(R_p)^2 = (x_a)^2 + (y_a)^2 \tag{42}$$

We assume that the angles change at a constant rate that depends on the path length for the vehicle. Given initial values for the angles (η, ϕ_p, and σ), we use the measured data for the distance (D) and the measured data for the change in vehicle position (dp) to estimate the changes in the angles ($d\phi_p$ and $d\sigma$). The initial and final values for ϕ_p were measured: the initial value for the first case was 90 degrees and the final value was 35.283 degrees. We do not have a method to measure η and σ. We made a drawing of the initial and final configurations. We estimate that the initial values were: σ = 30 degrees and η = -60 degrees and the final values were: σ = 0 degrees and η = -144.717 degrees.

We use the measured data for the distance (D) and the current value for σ to calculate R_p. Given the measured data for the change in vehicle position (dp), we estimate the changes in the angles ($d\phi_p$ and $d\sigma$):

$$d\phi_p = \alpha\ dp/R_p \tag{43}$$

$$d\sigma = \beta\ dp/R_p \tag{44}$$

where the slip factor (α) and the twist factor (β) are determined by numerical iteration. In Table 3, the vehicle reckoned that the change in orientation was -54.717 degrees, while the measured change in orientation was -47.899 degrees. We expect the slip factor to be approximately equal to the ratio of these two values (0.8754). Our estimate of the slip factor is: = 0.9188. The twist factor is used to reduce the angle σ from its initial value to its final value. Our estimate of the slip factor is: = 0.5754.

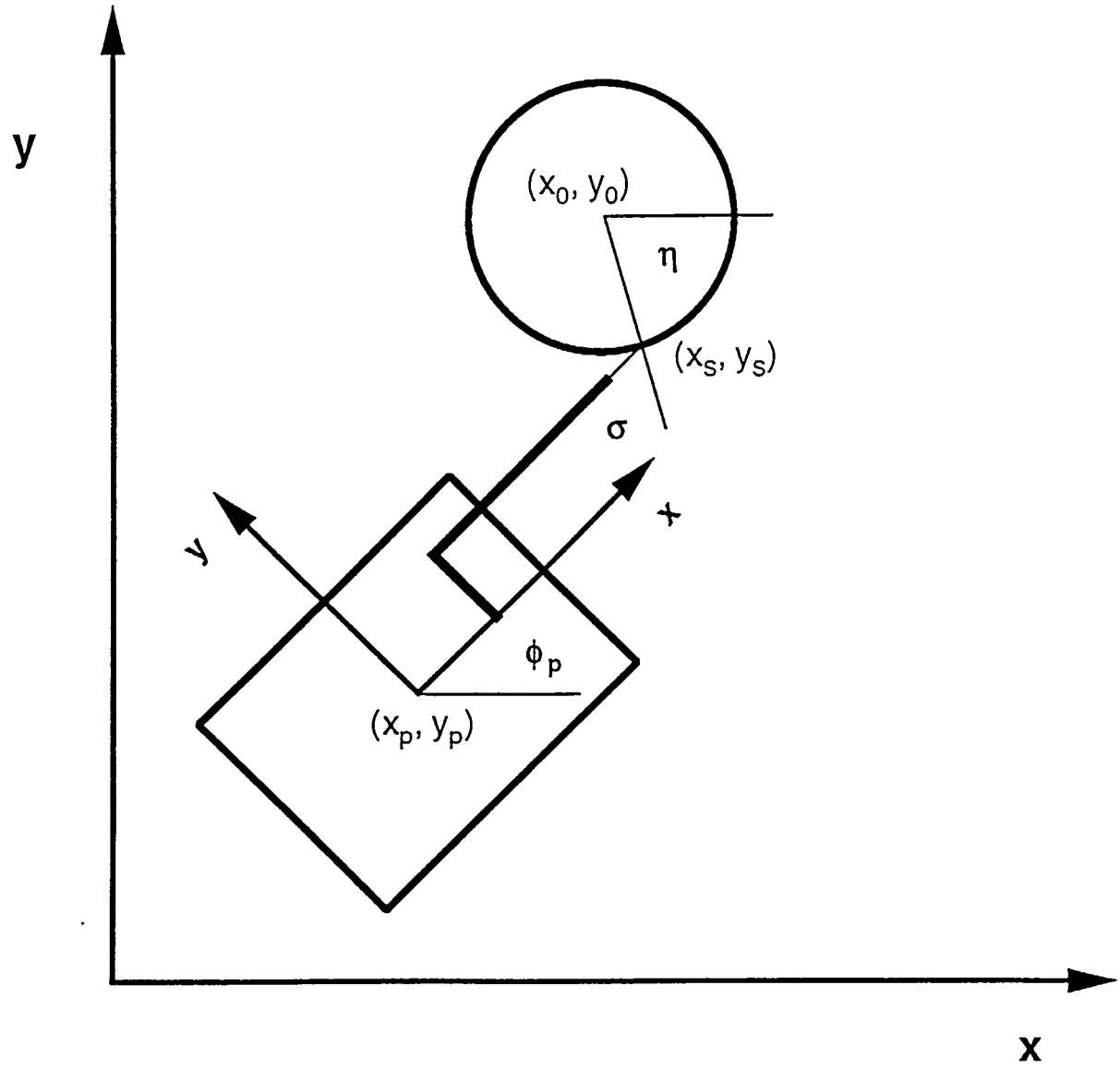

Fig. 29. Motion of the vehicle during the single pass experiments.

We have described the calculation that was used to calculate the Barrel Calc and Vehicle Calc curves in Fig. 12. We have calculated the radii and centers for the four curves in Fig. 12. The results are displayed in Table 4 and plotted in Fig. 30. Our goal for the center of the vehicle path (point C) was near the center of the barrel (point B). However, the center of our estimate of the vehicle path (point A) is a substantial distance (486 mm) from the goal (point C).

Table 4. The Radii and Centers for the Four Curves in Fig. 12. The Units are meters.

Curve	R	x_0	y_0
Barrel Calc	0.290	5.499	5.906
Barrel Data	0.098	5.548	5.683
Vehicle Calc	2.326	5.571	6.285
Vehicle Data	1.858	5.540	5.800

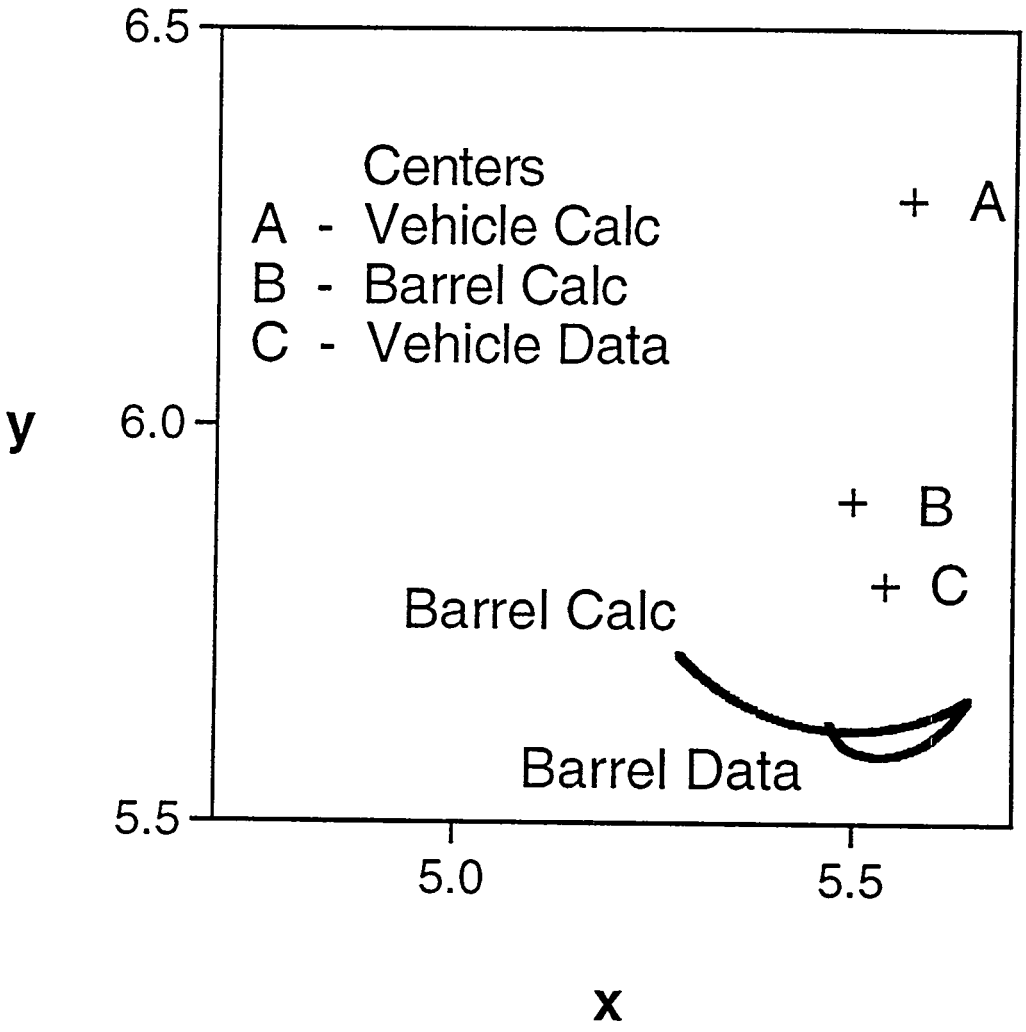

Fig. 30. Experimental and calculated data for the barrel surface and the centers for three arcs. The units of x and y are meters.

Figure 31 is a plot of the arm orientation (ϕ_p) at several points on the barrel during the experiment. The arm begins on the right at a 90 degree angle (in the world coordinate system) and finishes on the left at a 42 degree angle.

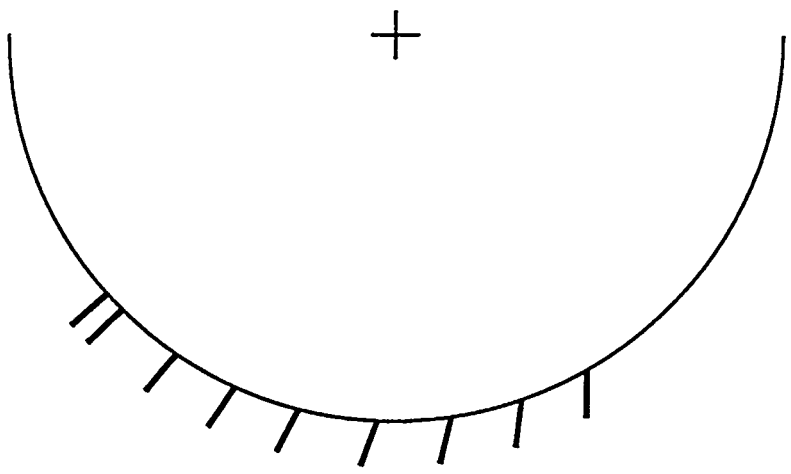

Fig. 31. The arm orientation (ϕ_p) at several points on the barrel during the experiment.

INTERNAL DISTRIBUTION

1-5. J. E.Baker
6. J. Barhen
7. M. Beckerman
8. C. W. Glover
9-13. W. C. Grimmell
14. J. N. Herndon
15. J. P. Jones
16. H. E. Knee
17-21. R. C. Mann
22. E. M. Oblow
23. C. E. Oliver
24. L. E. Parker
25-29. F. G. Pin
30. N. S. V. Rao
31-35. D. B. Reister
36. S. L. Schrock
37. S. Shekhar
38-42. R. F. Sincovec
43. E. C. Uberbacher
44-48. M. A. Unseren
49. R. C. Ward
50. EPMD Reports Office
51-52. Laboratory Records Department
53. Laboratory Records, ORNL-RC
54. Document Reference Section
55. Central Research Library
56. ORNL Patent Office

EXTERNAL DISTRIBUTION

57. Dr. Peter Allen, Department of Computer Science, 450 Computer Science, Columbia University, New York, NY 10027
58. Dr. John Baillieul, Aerospace and Mechanical Engineering Department, Boston University, 110 Cummington St., Boston, MA 02215
59. Dr. Wayne Book, Department of Mechanical Engineering, J. S. Coon Building, Room 306, Georgia Institute of Technology, Atlanta, GA 30332
60. Professor Roger W. Brockett, Harvard University, Pierce Hall, 29 Oxford St., Cambridge, MA 02138
61. Dr. Steven Dubowsky, Department of Mechanical Engineering, Massachusetts Institute of Technology, Building 3, Room 469A, 77 Massachusetts Ave., Cambridge, MA 02139
62. Professor Donald J. Dudziak, Dept. of Nuclear Engineering, 110B Burlington Engineering Labs, North Carolina State University, Raleigh, NC 27695-7909
63. Mr. Steve Holland, Robotics, B/MD-63, General Motors Corporation, NAO Manufacturing Center, 30300 Mound Rd., Warren, MI 48090-9040
64. Dr. Avi Kak, Department of Electrical Engineering, Purdue University, Northwestern Ave., Engineering Mall, Lafayette, IN 47907
65. Professor Takeo Kanade, Computer Science and Robotics, Carnegie Mellon University, Pittsburgh, PA 15213-3890
66. Dr. James E. Leiss, Route 2, Box 142C, Broadway, VA 22815-9303
67. Dr. Oscar P. Manley, Division of Engineering, Mathematical, and Geosciences, Office of Basic Energy Sciences, ER-15, U.S. Department of Energy - Germantown, Washington, DC 20545
68. Professor Neville Moray, Department of Mechanical and Industrial Engineering, University of Illinois, 1206 West Green St., Urbana, IL 61801
69. Dr. Wes Snyder, Department of Radiology, Bowman Gray School of Medicine, N.C. Baptist Hospital School of Medicine, 300 S. Hawthorne Dr., Winston-Salem, NC 27103
70. Professor Mary F. Wheeler, Department of Mathematical Sciences, Rice University, P.O. Box 1892, Houston, TX 77251

71. Office of Assistant Manager for Energy Research and Development, U.S. Department of Energy, Oak Ridge Operations Office, P.O. Box 2001, Oak Ridge, TN 37831-8600
72-73. Office of Scientific and Technical Information, P.O. Box 62, Oak Ridge, TN 37831